Chem Soc Rev

ROYAL SOCIETY OF CHEMISTRY

REVIEW ARTICLE

View Article Online
View Journal | View Issue

Check for updates

Cite this: *Chem. Soc. Rev.*, 2023, **52**, 4725

Polypyridyl Ru(II) or cyclometalated Ir(III) functionalized architectures for photocatalysis

Yan-Lin Li,[a] Ai-Juan Li,[a] Sheng-Li Huang, *[a] Jagadese J. Vittal *[b] and Guo-Yu Yang*[a]

Received 23rd March 2023

DOI: 10.1039/d3cs00053b

rsc.li/chem-soc-rev

The chemistry of polypyridyl Ru(II) and cyclometalated Ir(III) derivatives provides long-lasting interest to researchers due to the inherent advantage of their triplet states in a variety of photoactivities. The introduction of Ru(N^N)$_3$ and Ir(C^N)$_2$(X^N) modules into well-defined architectures extends the research areas of both photoactive metal complexes and network chemistry, generating a lot of new opportunities with interesting structural aesthetics and profound functional possibilities. The rapid development of research in integrating Ru(II) or Ir(III) metallotecons into the architectures has been apparent in recent years which makes this a fascinating subject for reviewing. This review focuses on the design and syntheses of Ru(N^N)$_3$ and Ir(C^N)$_2$(X^N) functionalized architectures of metal–organic frameworks (MOFs), covalent–organic frameworks (COFs), metallasupramolecules, organic supramolecules and supramolecular organic frameworks (SOFs). Furthermore, the photocatalytic applications including the hydrogen evolution reaction (HER), carbon dioxide reduction reaction (CO$_2$RR), photocatalytic oxidation and photoredox catalysis of organic transformation are also presented.

1. Introduction

The octahedral d^6-metal complexes, namely, polypyridyl–Ru(II) and cyclometalated–Ir(III) complexes have been exploited in photonic and optoelectronic applications due to their interesting electronic transitions and furthermore, charge-transfer of their triplet states is tunable over a wide range.[1,2] Specifically, Ru(N^N)$_3$ and Ir(C^N)$_2$(X^N) (X = C or N), where (N^N) and (C^N) respectively represent the diimine ligand and cyclometalated ligand, have been mostly utilized for this purpose since the presence of Ru(II) and Ir(III) enhances the spin–orbit coupling and promotes the intersystem crossing of electrons from the excited singlet state to the triplet state, and their excited states are simultaneously influenced by the metal-to-ligand charge transfer (MLCT) and intraligand charge transfer (LLCT).[3] The bonding of d^6-metal ions and coordinating units provide enormous possibilities for assembling intriguing photoactive metal complexes.[4,5] The highest occupied

Yan-Lin Li

Yan-Lin Li received her BS degree (2015) and MS degree (2018) from the China University of Petroleum. She is currently a PhD candidate under the supervision of Prof. Sheng-Li Huang at the Beijing Institute of Technology. Her current research interests are the preparation of polypyridyl Ru(ii) or cyclometalated Ir(iii) functionalized COFs for photocatalysis.

Ai-Juan Li

Ai-Juan Li is currently a PhD candidate under the supervision of Prof. Sheng-Li Huang at the Beijing Institute of Technology. Her current research interests are the preparation of polyoxometalate functionalized architectures, and polypyridyl Ru(ii) or cyclometalated Ir(iii) based supramolecular architectures for photocatalysis.

---

[a] *MOE Key Laboratory of Cluster Science, Beijing Key Laboratory of Photoelectronic/Electrophotonic Conversion Materials, School of Chemistry and Chemical Engineering, Beijing Institute of Technology, Beijing 100081, China. E-mail: huangsl@bit.edu.cn, ygy@bit.edu.cn*

[b] *Department of Chemistry, National University of Singapore, 3, Science Drive 3, Singapore 117542, Singapore. E-mail: chmjjv@nus.edu.sg*

molecular orbital (HOMO) –lowest unoccupied molecular orbital (LUMO) gap, light absorption region, triplet lifetime, excitation potential, emission quantum yields (Φ_{PL}) and other optoelectronic characteristics are readily modulated *via* substituent modification of the (C^N) and (N^N) units. The strong visible light absorption capacity and stable long-lived photoexcited states of Ru(N^N)$_3$ and Ir(C^N)$_2$(X^N) derivatives enabled their wide application in photophysics and photochemistry fields.[6,7] For example, photoexcited Ir(ppy)$_3$ (H-ppy = 2-phenylpyridine) exhibits special reducing features in photosynthesis owing to the strong electron-donating power of three ppy anions.[8] Ru(N^N)$_3$ and Ir(C^N)$_2$(X^N) units have reliable synthesis and high chemical stability, and hence, their combinations with elaborate synthons yield desirable architectures with great significance in both skeletons and photofunctions (Fig. 1).

In the past two decades, well-defined architectures of MOFs,[9–12] COFs,[13–15] metallasupramolecules,[16–18] organic supramolecules[19–21] and SOFs[22–25] have received greater attention due to their rich and designable structures, modifiable pore space and tunable functionality.[26] These architectures provide the best models for the structure–property relationship study, and the well-organized skeletons commonly possess special functions for olefin separation in hierarchical porous MOFs[27,28] for enzyme separation in mesoporous COFs,[29,30] for unusual reactions in metallasupramolecules which act as molecular flasks,[31] for photodynamic therapy efficacy in organic supramolecules[32] and for accessible film production in SOFs.[33] Like building skyscrapers, the molecular architectures can be precisely constructed by the judicious choice of divergent building blocks.[34] The combination of the octahedral core of d^6-metal ions and peripheral coordination components produces various three-dimensional (3D) building blocks,[35,36] that may not be possible with pure organic components alone (Table 1). Furthermore, incorporation of Ru(N^N)$_3$ and Ir(C^N)$_2$(X^N) into well-defined architectures will not only yield unexpected and unusual properties of these materials but is also expected to have synergistic effects. For example, the structural confinement of the Ru(N^N)$_3$ or Ir(C^N)$_2$(X^N) moieties in MOFs, produced new photofunctional entities due to the weak conjugation of crystalline coordination frameworks.[72] In photocatalysis, photogenerated charges are easily separated and transferred to Lewis acid sites for redox reactions.

Efficient utilization of solar energy is an important way to solve the current global energy shortage and environmental crisis, and furthermore, photocatalysis can accomplish the transformation of the abundant solar energy into chemical energy.[73] Molecular Ru(N^N)$_3$ and Ir(C^N)$_2$(X^N) complexes have been widely employed in various photosynthesis reactions, such as the HER,[74,75] CO$_2$RR,[76–78] water oxidation,[79,80] and particularly in organic transformations including electron transfer reactions, H atom transfer reactions and energy transfer reactions.[81–83] Ru(N^N)$_3$ and Ir(C^N)$_2$(X^N) functionalized architectures exhibit numerous applications from luminescence,[7,84,85] sensing,[86] solar fuels[87,88] to bioimaging[89–91] and furthermore, photocatalytic activity is always the most intriguing performance.[92–98] They have great advantages in the photocatalysis system due to the following: (1) their light adsorption ranges are tunable from visible light to the near-infrared region.[6,99] The integration of Ru(II)/Ir(III)–metallotecons within the architectures can broaden the spectral region,

Sheng-Li Huang

*Sheng-Li Huang received his PhD in chemistry in 2013 from Fudan University. Then he worked as a research scientist at the Institute of Materials Research & Engineering of A*STAR in Singapore. At the beginning of 2018, he moved to the Beijing Institute of Technology. His research interests contain well-organised architectures, functional polyoxometalates, Ru (Ir) chemistry and photosynthesis.*

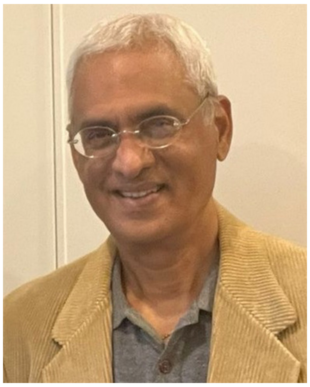

Jagadese J. Vittal

Jagadese J. Vittal obtained his PhD from the Indian Institute of Science, Bangalore (1982). He was a postdoctoral research associate and service crystallographer at the University of Western Ontario, Canada, before moving to NUS as a faculty member in 1997. He has been an Emeritus Professor since 2021. JJ is interested in solid-state science and structural chemistry including new materials, chemical reactivities, and structure–property relationships.

Guo-Yu Yang

Guo-Yu Yang received his MS and PhD degrees from Jilin University in 1991 and 1998, respectively. During the period 1998–2001, he worked as a Postdoctoral Fellow at the University of Notre Dame and Stockholm University. He became a full professor at FJIRSM-CAS in 2001. He was awarded the Cheung Kong Professorship in 2009. In 2014, he moved to the Beijing Institute of Technology. His research interests include oxo cluster chemistry and function development of oxo clusters.

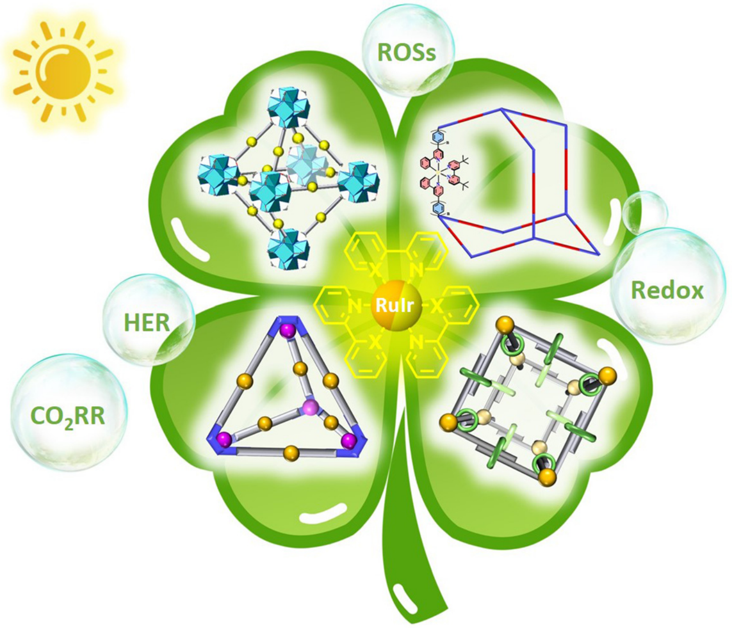

Fig. 1 $Ru(N\hat{}N)_3$ or $Ir(C\hat{}N)_2(X\hat{}N)$ functionalized architectures and their photocatalytic applications.

providing a platform for the efficient utilization of solar energy. (2) In these architectures, the varied potentials of building units linked to Ru(II)/Ir(III)-metallotecons lead to the efficient separation of photogenerated electrons and holes.[100–102] (3) The conjugation of architectures is beneficial for highly efficient charge transfer, and the porous frameworks permitting more substrate to access the surface of the architectures and increase the utilization of charges.[103] (4) Such architectures provide the required nano-space to govern the host–guest optoelectronic interactions, which accelerates photocatalysis arising from the photophysical interaction between bound guests and the emitting hosts. The nano-space can also accommodate other nanoparticles, producing interesting catalytic performance *via* the synergistic effect.[70,104,105] (5) Most of these architectures are insoluble in common solvents, hence these noble metal catalysts can be easily recycled and reused.[106] (6) These designed architectures are expected to provide a meaningful structure–function relationship which will help to design better catalysts and to improve our understanding of the catalytic process.[54] Although some types of classical photocatalysts have been well explored, they have their disadvantages and limitations. Organic dyes have a tunable visible light absorption area, but they are readily decomposed during use.[107,108] The cheap inorganic semiconductors of TiO_2, Bi_2WO_6, α-Fe_2O_3, CdS and ZnO have better photostability, however the unavailable synthesis of nanoparticles without surfactant, narrow absorption spectrum of sunlight, high reduction potential, inefficient photogenerated charge separation and toxicity, in some cases restrict their wide application. The construction of heterojunctions and Schottky junctions led by doping of precious metals could improve some photochemical characteristics,[109–111] but suffer from aggregation and deactivation of precious metals.[112] In sharp contrast to other emerging photocatalysts, such as organic polymers, inorganic–organic hybrid materials, MOFs or COFs assembled from net organic building modules, the necessary conditions for photocatalysis including light absorption capacity, charge separation and utilization efficiency, interaction between substrate and catalyst of $Ru(N\hat{}N)_3$ and $Ir(C\hat{}N)_2(X\hat{}N)$ functionalized architectures could be greatly improved.

This review is focused on the design and synthesis of $Ru(N\hat{}N)_3$ and $Ir(C\hat{}N)_2(X\hat{}N)$ containing architectures, which will be presented and discussed in separate sections based on MOFs, COFs, metallasupramolecules, organic supramolecules and SOFs. The $Ru(N\hat{}N)_3$ and $Ir(C\hat{}N)_2(X\hat{}N)$ units can be obtained *via* reliable synthetic routes, the incorporation of these units into well-defined architectures commonly involves two methodologies (Fig. 2),[113] *viz.* deployment of the metalloligands[70,71,114] and post-synthetic modification (PSM).[115–118] High chemical stability of the $Ru(N\hat{}N)_3$ and $Ir(C\hat{}N)_2(X\hat{}N)$ units makes the synthesis viable by the first method, even under harsh reaction conditions such as strong base or acid environments and high temperature. The post-synthetic incorporation of $Ru(N\hat{}N)_3$ and $Ir(C\hat{}N)_2(X\hat{}N)$ units are achieved by the coordination linkage of $(N\hat{}N)$ groups from the skeleton with $Ru(N\hat{}N)_2$- or $Ir(C\hat{}N)_2$- precursor. These architectures have many photocatalytic applications. The HER, CO_2RR, photocatalytic oxidation and photoredox catalysis of organic transformation are concluded.

Table 1 Structural diversity of Ru(N^N)$_3$ and Ir(C^N)$_2$(X^N) cores (AS = Active Site)

No. of AS	Structure diagram	Specific structure	Ref.
1		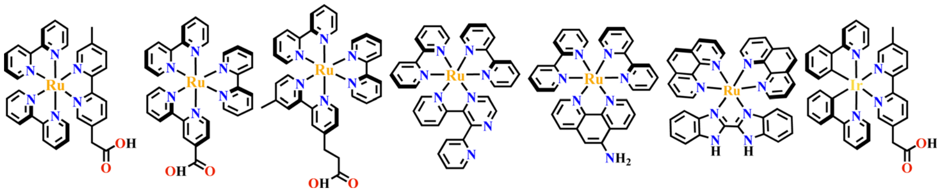	37–42
2		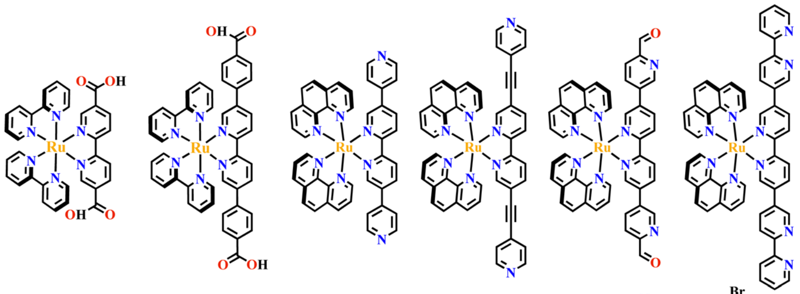	43–46
		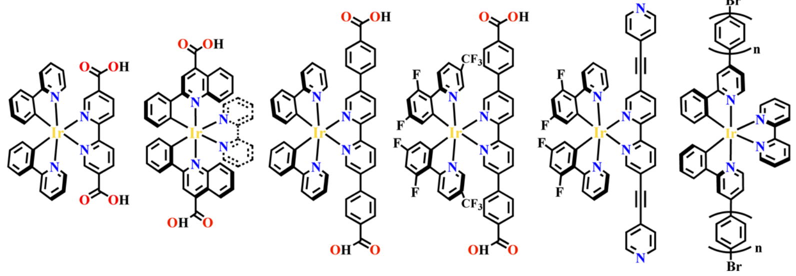	47–52
3	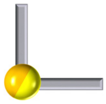	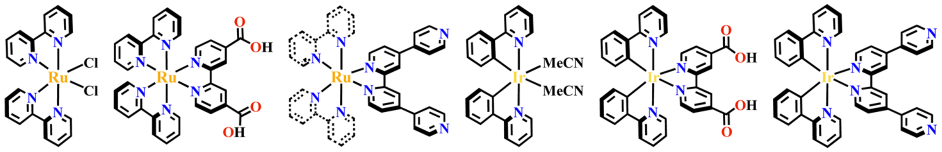	53–58
	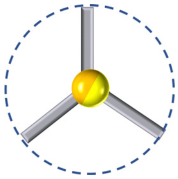	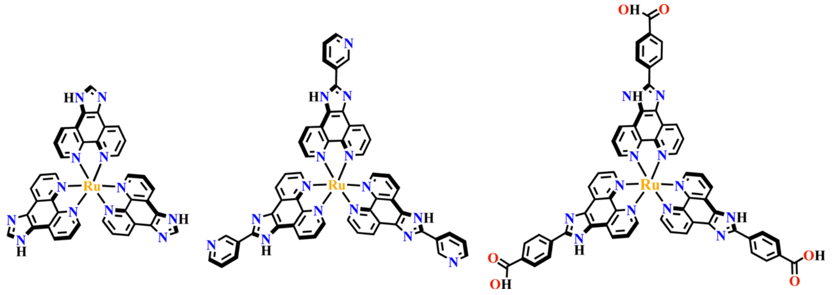	59–61
	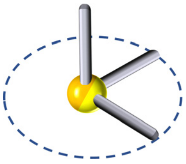	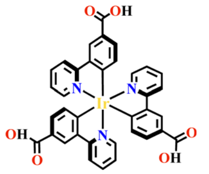	62
	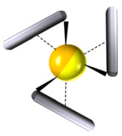	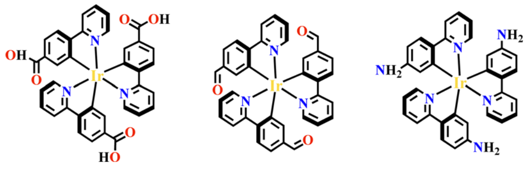	63–65

Table 1 (*continued*)

No. of AS	Structure diagram	Specific structure	Ref.
4	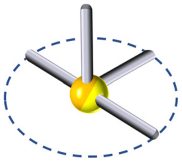	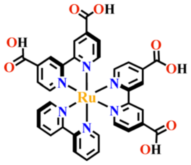	66
	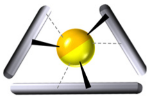	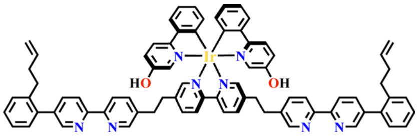	67
6	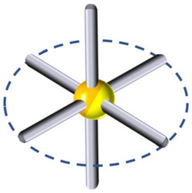	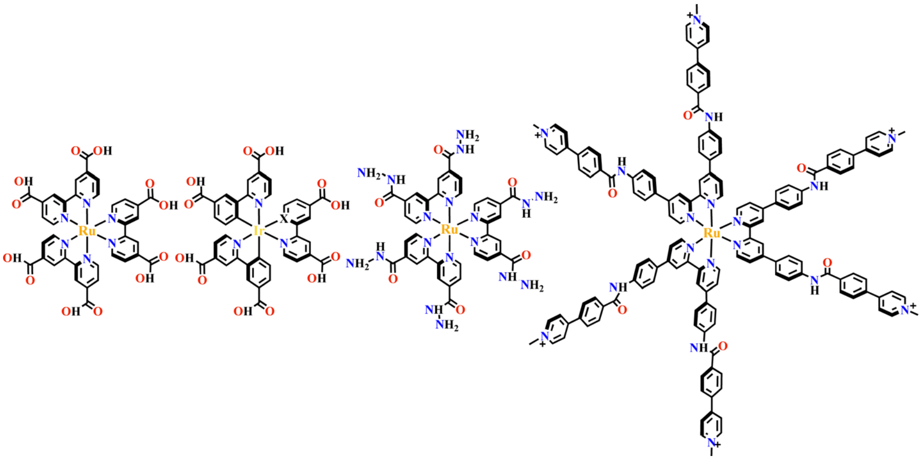	35 and 68–70
	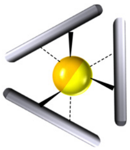	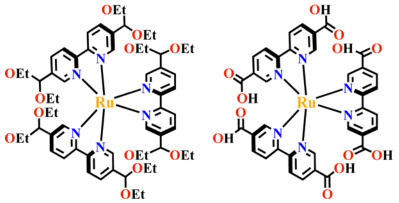	68 and 71

2. Ru(N^N)$_3$ or Ir(C^N)$_2$(X^N) functionalized MOFs

MOF, also known as porous coordination polymer, is one of the fastest growing research fields in both chemistry and materials science in the last two decades.[34,119–123] The structural diversity, ultrahigh surface area, crystalline skeleton and tunable functionality allow MOFs to be widely utilized in various disciplines.[124–131] As featuring periodic networks, MOFs are formed by the self-assembly of organic linkers with metal ions or metal clusters (secondary building units (SBUs)).[34] A large number of MOFs have been reported arising from different types of organic linkers, variable coordination numbers and flexible coordination modes of metal ions, as well as the *in situ* formed "OH$^-$" and "O^{2-}" species leading to the formation of wide-ranging MOFs.[132,133] A judicious combination of organic linkers and SBUs control the topology of the resulting MOFs, whose photofunctions are commonly inherited from the photo-responsive ligands or post-introduced photosensitizers.[34,134] In general, Ru(N^N)$_3$ and Ir(C^N)$_2$(X^N) functionalized MOFs are synthesized by two routes: (1) direct reaction of metalloligands with metal ions.[35,49,135–140] (2) PSM: the bis-chelating sites of ligand skeleton in the MOFs, such as (N^N) groups, could be bonded to the Ru(II) or Ir(III) precursors, thus producing MOFs containing Ru(N^N)$_3$ or Ir(C^N)$_2$(X^N) units.[50,141,142] In addition, the metalloligand could also be anchored at the unsaturated coordination sites of the MOFs *via* PSM.[37,118] In the syntheses of Ru(N^N)$_3$ and Ir(C^N)$_2$(X^N) functionalized MOFs, the nature of metal ions has great influence on the SBUs, topology and function of the resulting MOFs. In the following section, the photoactive MOFs will be divided into three categories according to the metal ion species in the SBUs, *viz.* 3d metal ions, d^0 metal ions and 4f metal ions.

2.1 Photoactive MOFs constructed from the 3d metal ions

Transition metals of Mn^{2+}, Fe^{2+}, Co^{2+}, Ni^{2+}, Cu^{2+} and Zn^{2+}, have been commonly used in the construction of various MOFs with the following advantages: (1) the variable coordination numbers and flexible coordination modes of these transition metal ions provide different SBUs for the construction of diverse

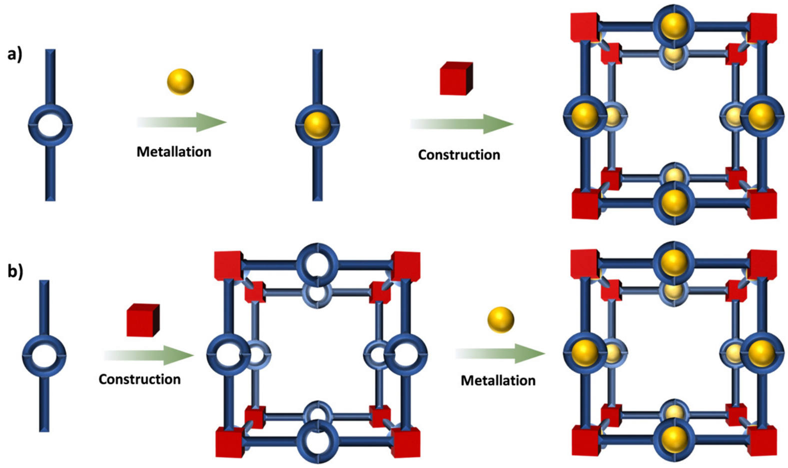

Fig. 2 Two synthetic strategies for metalloarchitectures: (a) metalloligands; (b) PSM.

MOFs; (2) the reaction conditions of solvents, acid or base, and temperature have great influence on the formation of metal nodes, providing infinite possibilities to synthesize different SBUs; (3) weak metal–ligand interactions facilitate the crystallization of the MOFs. But most of MOFs incorporating transition metal ions have low chemical stability, which has adverse effects on the catalytic applications. However, these reactions produce photoactive MOFs with diverse structures and interesting functions.

A combination of Ru(II) and phenba (phenba = 4-(1*H*-imidazo[4,5-*f*][1,10]phenanthrolin-2-yl)benzoic acid) formed a C_3 symmetric tridentate metalloligand $[Ru(phenba)_3]^{2+}$. The reaction of $[Ru(phenba)_3]^{2+}$ with $Co(NO_3)_2$ produced **[Ru(phenba)$_3$+Co]-MOF** with two-dimensional (2D) hexagonal layers and large open channels. Mesoporous **[Ru(phenba)$_3$+Co]-MOF** exhibited a selective gas sorption property, and its CO_2 sorption capacities were far better than N_2 (Fig. 3).[61] **[Ru(ip)$_3$+Co]-MOF** (Hip = 1*H*-imidazo[4,5-*f*][1,10]phenanthroline) revealed a high symmetry *ctn* network consisting of 3-connected $[Ru(ip)_3]^{2+}$ and 4-connected Co^{2+} units. Under visible light, the overall conversion of CO_2 reduction and H_2O oxidation was achieved simultaneously by this multifunctional photocatalyst with a high conversion rate and CO selectivity.[59] Ir(C^N)$_3$-carboxy metalloligand was synthesized in a stepwise manner from the cyclometallation of (C^N)-ester derivatives and Ir(III) precursor, and then ester hydrolysis. Ir(C^N)$_3$-cores have two stereochemical forms, namely, *mer* and *fac*. The *fac* isomer has better stability and a longer emission lifetime than *mer*, and in *fac*-isomer all nitrogen atoms are *trans* to carbon atoms. The introduction of a carboxy group into the *para*-position of the coordinated C or N atoms, resulting in the bowl shaped metalloligand, whose carboxy groups are nearly perpendicular to each other. Using the Ir(ppy-COOH)$_3$-metalloligand, (H-ppy-COOH = 3-(pyridin-2-yl)benzoic acid) **[Ir(ppy-COO)$_3$+Co]-MOF** and **[Ir(ppy-COO)$_3$+Zn$_4$]-MOF** were synthesized. **[Ir(ppy-COO)$_3$+Co]-MOF** was applied as an efficient O_2-evolution–reaction electrocatalyst.[62] The highly phosphorescent **[Ir(ppy-COO)$_3$+Zn$_4$]-MOF** was used in O_2 sensing[63] as well as photocatalytic pollutant degradation.[143] The position of the carboxyl groups at Ru(N^N)$_3$[38,66,144] and Ir((C^N))$_2$(N^N)-metalloligands can influence the topology of MOFs.[57,145]

In (C^N)-derivatives, the introduction of the carboxy groups into both the *para* positions of the coordinated C and N generated the hexadentate ligands Ir(H$_2$dcppy)$_3$ and [Ir(H$_2$dcppy)$_2$(H$_2$dcbpy)]$^+$ (H-H$_2$dcppy = 2-(3-carboxyphenyl)pyridine-4-carboxylic acid, H$_2$dcbpy = 2,2′-bipyridine-4,4′-dicarboxylic acid), and the carboxy groups of these two octahedral metalloligands linked with linear mono-node $[Ni(cyclam)]^{2+}$ and formed the two isostructural complexes **[Ir(dcppy)$_3$+Ni]-MOF** and **[Ir(dcppy)$_2$(dcbpy)+Ni]-MOF** with *pcu* topology. They were 2-interpenetrating networks and exhibited a good CO_2/N_2 separation property (Fig. 4).[35]

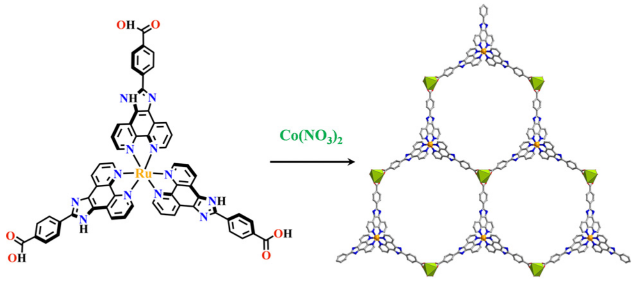

Fig. 3 **[Ru(phenba)$_3$+Co]-MOF**.[61]

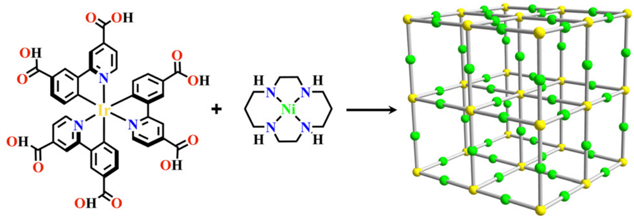

Fig. 4 **[Ir(dcppy)$_3$+Ni]-MOF**.[35]

2.2 Photoactive MOFs constructed from d^0 metal ions

The d^0 metal ions of Ti^{4+}, Zr^{4+} and Hf^{4+} have high charge density and strong oxophilicity, and they have a particularly strong bonding ability with carboxylate groups. These d^0 metal salts can easily form metal hydroxides or oxides when encountering water, further increasing the chemical stability of metal-carboxylate clusters. The MOFs synthesized from Ti^{4+}, Zr^{4+} or Hf^{4+} have strong chemical stability and their skeletons are maintained even under a strong acid environment. They are commonly used as heterogeneous catalysts based on their stable and porous frameworks. The strong metal-carboxylate interactions result in a lower control over the crystallization process, and difficulty in growing the single crystals suitable for X-ray diffraction was encountered.[146] Many d^0 metal-based MOFs exhibited versatile catalytic reactions. The bonding energy between Zr^{4+} and carboxylate groups was weaker than Ti^{4+} but stronger than Hf^{4+}, hence Zr_6-MOFs have medium levels of chemical stability and crystallization ability, promoting the rapid development of functional Zr_6-MOFs.[146–148] The reaction of Zr^{4+} and COO^- groups unexpectedly afford a $Zr_6(\mu_3\text{-}O)_4(\mu_3\text{-}OH)_4(CO_2)_{12}$ cluster.

Zhou and co-workers reported the synthesis of mesoporous MOFs, termed **(TPTB+Zr$_6$)-MOF** (H_4TPTB = 5′,5′′′-bis(4-carboxylatophenyl)-4′′′,6′-dimethoxy-[1,1′:3′,1′′:4′′,1′′′:3′′′,1′′′′-quinquephenyl]-4,4′′′′-dicarboxylate), *via* assembling the Zr_6 clusters with the tetratopic carboxylate linkers H_4TPTB. The carboxylate group of $[Ru(bpy)_2(H_2bpydc)]^{2+}$-metalloligand ($H_2$bpydc = 2,2′-bipyridine-5,5′-dicarboxylic acid) linked to the uncoordinated sites of the Zr_6 cluster, leading to photoactive **Ru(bpy)$_2$(bpydc)@(TPTB+Zr$_6$)-MOF** with the expected porous network. It showed high catalytic efficiency in the aza-Henry reaction (Fig. 5).[118]

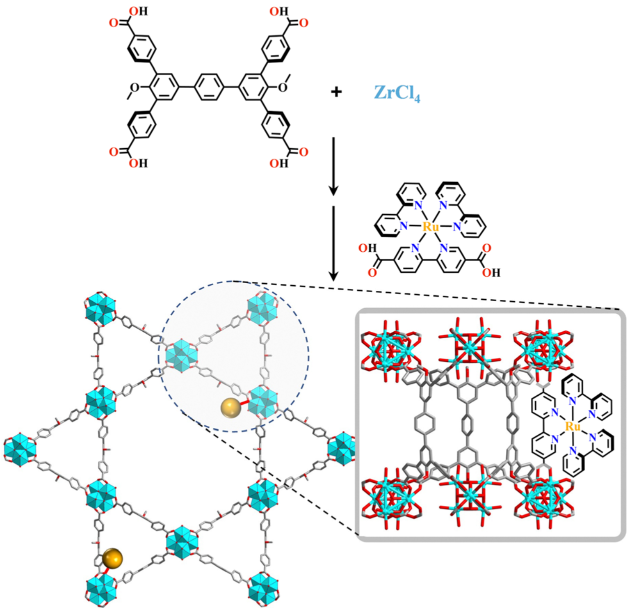

Fig. 5 Ru(bpy)$_2$(H$_2$bpydc)-metalloligand-functionalized **(TPTB+Zr$_6$)-MOF**.[118]

In the construction of Ru(N^N)$_3$ and Ir(C^N)$_2$(X^N) functionalized MOFs, the most popular synthetic method was the direct reaction of metalloligand and metal source. In this way, the structural advantages of Ru(N^N)$_3$ or Ir(C^N)$_2$(X^N) units could be passed to the target frameworks and the photoactive units could be well organized in the pore. Using metalloligand $[Ru(bpy)_2(H_2bpydc)]$ and 4,4′-biphenyldicarboxylic acid (H_2bpdc), Lin and co-workers synthesized several heteroleptic MOFs that were isostructural with UIO-67 and exhibited high photocatalytic activity in aza-Henry reactions.[43] The introduction of $Cu(H_xPO_4)_y$ into **Cu@[Ru(bpy)$_2$(bpydc)/bpdc+Zr$_6$]-MOF** produced the dual-functional catalyst **Cu@[Ru(bpy)$_2$(bpydc)/bpdc+Zr$_6$]-MOF**, and it promoted the conversion of CO_2 to C_2H_5OH with light irradiation and CH_3OH in the absence of light. TEM analysis showed that the catalysts formed Cu^0 nanoparticles in the dark, which were the active species for CO_2 transformation to CH_3OH. With light illumination, $\{[Ru(bpy)_2(bpydc)]^{2+}\}^*$ transferred e^- to Cu^{2+} and generated Cu^+, simultaneously, $\{[Ru(bpy)_2(bpydc)]^{2+}\}^*$ was quenched by electron injection from Cu^0 and generated Cu^+, which were responsible for C_2H_5OH production.[138] The encapsulation of $[Ni(bpet)(H_2O)_2]^{2+}$ (bpet = 1,2-bis[(pyridin-2-ylmethyl)thio]ethane) into **[Ru(bpy)$_2$(bpydc)/bpdc+Zr$_6$]-MOF** produced **Ni⊂[Ru(bpy)$_2$(bpydc)/bpdc+Zr$_6$]-MOF**, and the photogenerated electron reduced the Ni center with enhanced CO_2 affinity and formed a Ni–CO_2 adduct, achieving highly efficient CO_2 transformation with good CO selectivity.[139] Zhang and co-workers synthesized **Co@[Ru(bpy)$_2$(bpydc)/bpdc+Zr$_6$]-MOF** by the insertion of Co^{2+} as a single-site catalyst in the open (N^N)-sites of **[Ru(bpy)$_2$(bpydc)/bpdc+Zr$_6$]-MOF**, which supplied a molecular platform capable of rapid injection of multiple electrons from the photosensitizer to Co-catalyst, resulting in a MOF-based composite photocatalyst for efficient syngas production. The photogenerated electrons transferred from the photosensitizer to Co-catalyst, then reduced CO_2 and H_2O to syngas. In the photocatalytic process, the H_2/CO ratios could be well controlled by adjusting the water content or the ratio of PS/Cat in the MOFs.[149]

In the construction of Ru(N^N)$_3$-(UIO-67), the Ru(N^N)$_3$-metalloligand was simultaneously used with other linear dicarboxylate linkers because the small cavity in UIO-67 could not accommodate Ru(N^N)$_3$-units due to its small pore size. This problem was overcome by increasing the length between two terminal carboxyl groups of the metalloligands, producing more space for the accommodation of Ru(N^N)$_3$ or Ir(C^N)$_2$(X^N) units inside the framework. The linkage of $Ru(bpy)_2(H_2bpydc)$-metalloligands and $[Zr_6(\mu_3\text{-}O)_4(\mu_3\text{-}OH)_4]$-SBUs produced **Ru(bpy)$_2$(dbpydc)-Zr$_6$-MOF** ($H_2$dbpydc, 4,4′-([2,2′-bipyridine]-5,5′-diyl)dibenzoic acid). In the synthetic procedure, the addition of Wells–Dawson $\{P_2W_{18}\}$ polyoxometalates (POMs) resulted in the formation of **{P$_2$W$_{18}$}⊂[Ru(bpy)$_2$(dbpydc)+Zr$_6$]-MOF** (Fig. 6).[114] **{Ni$_4$P$_2$}⊂[Ru(bpy)$_2$(dbpydc)+Zr$_6$]-MOF**, and **{Ni$_4$P$_2$}⊂[Ir(ppy)$_2$(dbpydc)+Zr$_6$]-MOF** were obtained *via* similar synthetic methods. Both **[Ru(bpy)$_2$(dbpydc)+Zr$_6$]-MOF** and **[Ir(ppy)$_2$(dbpydc)+Zr$_6$]-MOF** had the same topological network with UIO-67. The incorporation of the photosensitizer and

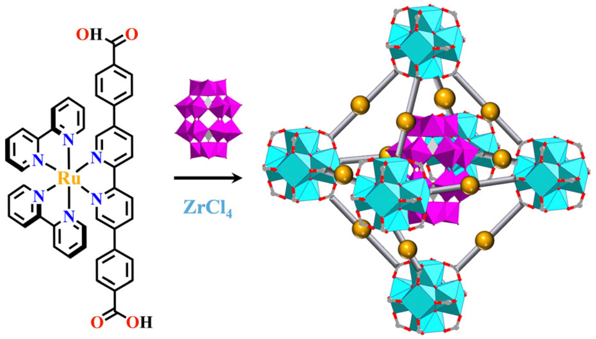

Fig. 6 $\{P_2W_{18}\}\subset$[Ru(bpy)$_2$(dbpydc)+Zr$_6$]-MOF.[114]

POMs $\{Ni_4P_2\}$ into a single framework shortened their distance, promoting the photo-generated electron transfer from photosensitizer to POMs, and the accumulation of electrons at POMs enhanced its reduction ability, thus achieving photocatalytic hydrogen production. However, **$\{Ni_4P_2\}\subset$[Ru(bpy)$_2$(dbpydc)+Zr$_6$]-MOF** could not photocatalyze hydrogen production because the Ru(N^N)$_3$ photosensitizer does not have a low enough reduction potential to permit electron accumulation at $\{Ni_4P_2\}$.[150] In POMs$\subset$Ru(Ir)-MOF, the enhanced multi-electron transfer from Ru(N^N)$_3$ or Ir(C^N)$_2$(X^N) photosensitizer to POMs catalyst was responsible for the photocatalytic hydrogen production.[114,150] Ye and co-workers synthesized a series of Ir(pqc)$_2$(N^N)-metalloligands (H-pqc = H-2-phenylquinoline-4-carboxylic acid), in which the (C^N)-units were located around the Ir(III) center with controllable *trans* arrangement and the carboxyl group was located at the *para* position of the N atom, resulting in linear [Ir(pqc)$_2$(N^N)]$^+$ metalloligands. The reaction of these metalloligands with $ZrCl_4$ yielded **[Ir(pqc)$_2$(N^N)+Zr$_6$]-MOF** (N^N derivatives = bpy, 4,4′-dimethoxy-2,2′-bipyridine, or 1,10-phenanthroline (phen)) which showed excellent photocatalytic activity in the selective sulfide oxidation under a O_2 atmosphere (Fig. 7).[48] The attachment of the (N^N^N)-unit with the carboxylate group produced similar metalloligands, such as [Ru(cptpy)$_2$]$^{2+}$ (cptpy = 4′-(4-carboxyphenyl)-terpyridine), and its combination with simple Zr-node produced 1D framework **[Ru(cptpy)$_2$+Zr]-MOF**, which had high stability and selectively photocatalyzed CO_2 to formate (HCOOH) under visible light irradiation.[151]

2D materials have unique photoelectric properties because the delamination has a great influence on their functions. Metal–organic layers (MOLs) are a new type of 2D organic–inorganic material.[152,153] They are highly dispersible and have enough exposed active sites.[154,155] A series of MOLs were constructed by linking Ir(C^N)$_2$(N^N)-[49,50,135,136,156,157] and Ru(N^N)$_3$-[44,158] metalloligands with SBUs of Hf$_{12}$ or Hf$_6$, exhibiting numerous applications. Ir(C^N)$_2$(N^N) or Ru(N^N)$_3$ derivatives are two efficient photosensitizers for the generation of $^1O_2$.[159,160] Hf atoms in the SBUs efficiently absorb X-rays and transfer its energy to Ir(C^N)$_2$(N^N) and Ru(N^N)$_3$ moieties, thus generating reactive oxygen species (ROSs) for photodynamic therapy. Hf$_6$-MOLs were synthesized from the reaction of $HfCl_4$ and H_3BPY (H_3BPY, 4′,6′-dibenzoato-[2,2′-bipyridine]-4-carboxylic acid), and the open (N^N)-coordination site of Hf$_6$-MOL was occupied by the reaction with [Ir(ppy)$_2$Cl]$_2$ or Ru(bpy)$_2$Cl$_2$. An X-ray excited Hf$_6$ cluster transferred energy to photosensitizer moieties, generating $^1O_2$.[156] The incorporation of POMs enhanced the generation of various ROSs. Under X-ray irradiation, different functional modules of **$\{P_2W_{18}\}\subset$[Ir(ppy)$_2$(dbpydc)+Hf$_{12}$]-MOL** synergistically produced the corresponding ROSs ($^\bullet$OH from Hf$_{12}$ cluster, $^1O_2$ from Ir-photosensitizer and O^{2-} from $\{P_2W_{18}\}$).[49] Similarly, **[Ir(dFCFppy)$_2$(dbpydc)+Hf$_{12}$]-MOL** (H-dFCFppy = 2-(2,4-difluorophenyl)-5-(trifluoromethyl)pyridine) and **Ir(dFCFppy)$_2$(N^N)@(BPY+Hf$_6$)-MOL** could simultaneously generate $^1O_2$ from the Ir(C^N)$_2$(N^N) unit and $^\bullet$OH from Hf$_6$ or Hf$_{12}$ SBUs.[50] The weakly coordinated trifluoroacetic acid of **[Ru(bpy)$_2$(dbpydc)+Hf$_{12}$]-MOL** was replaced by 2-(5′-methyl-[2,2′-bipyridin]-5-yl)acetic acid, which was further coordinated with M(CO)$_3$X (M = Mn or Re, X = Cl or Br), leading to **Re@[Ru(bpy)$_2$(dbpydc)+Hf$_{12}$]-MOL** or **Mn@[Ru(bpy)$_2$(dbpydc)+Hf$_{12}$]-MOL** with efficient photocatalytic CO_2RR activities. The photogenerated electrons transferred from the Ru(N^N)$_3$ photosensitizer to Mn or Re catalyst, and the coordination interaction between CO_2 and catalyst enhanced its electron grabbing capacity from the catalyst, enhancing the selective CO_2 transformation to CO.[155] Furthermore, **OTf@[Ir(dFCFppy)$_2$(dbpydc)+Hf$_{12}$]-MOL** (OTf = triflate) could effectively catalyse dehydrogenative cross-couplings. In this system, dehydrogenation occurred on [Ir(dFCFppy)$_2$(H$_2$dbpydc)]$^+$ bridging ligands, and the OTf on the Hf$_{12}$ SBUs working as Lewis acid.[136] When **[Ir(dFCFppy)$_2$(dbpydc)+Hf$_{12}$]-MOL** was decorated with Ni(2-(4′-methyl-[2,2′-bipyridin]-4-yl)acetate)Cl$_2$ at Hf$_{12}$ centers (Fig. 8), the corresponding **Ni@[Ir(dFCFppy)$_2$(dbpydc)+Hf$_{12}$]-MOL** showed high

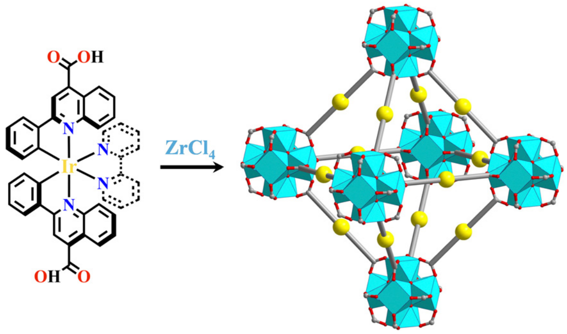

Fig. 7 [Ir(pqc)$_2$(N^N)+Zr$_6$]-MOF.[48]

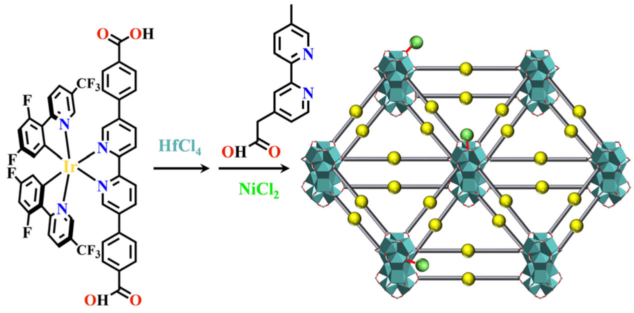

Fig. 8 Ni@[Ir(dFCFppy)$_2$(dbpydc)+Hf$_{12}$]-MOL.[135]

photoactivities in C–S, C–O, and C–C cross-coupling reactions.[135] **OTf/Co@[Ru(bpy)$_2$(dbpydc)+Hf$_{12}$]-MOL** hierarchically integrated three active sites into one complex, OTf as the strong Lewis acid, $[Ru(bpy)_2(H_2dbpydc)]^{2+}$ ligand as the photosensitizer, and [Co(dimethylglyoxime)$_2$(4-pyridinepropionate)]Cl as a hydrogen-transfer catalyst. They worked synergistically for tandem catalysis.[158]

In contrast to numerous Zr-MOFs and Hf-MOFs, only a few Ti-MOFs were reported because Ti^{4+} ions are easily hydrolyzed and strong Ti–carboxylate bonds make the crystallization of Ti-MOFs difficult.[146] The reaction of [Ti_6O_6(isopropoxy)$_6$(4-aminobenzoate)$_6$] and Ru(Ir)-metalloligand or 4,4′-biphenyldicarboxylic acid yielded **[Ru(bpy)$_2$(bpydc)/bpdc+Ti$_3$]-MOF** or **[Ir(ppy)$_2$(bpydc)/bpdc+Ti$_3$]-MOF**, and the combination of photosensitizer and Ti_3 cluster facilitated the photocatalytic HER under visible light.[140]

2.3 Photoactive MOFs constructed from 4f metal ions

Rare-earth elements possess rich optical, electrical, and magnetic properties due to their large atomic magnetic moment, unique 4f sublayer electronic structure, and strong spin–orbit coupling. Lanthanide (Ln) ions have flexible coordination modes, high coordination numbers, strong Lewis acid[142] and strong oxophilicity based on the Hard–Soft–Acid–Base theory.

A few Ru(N^N)$_3$ or Ir(C^N)$_2$(X^N) functionalized Ln-MOFs have been reported with interesting functions.[99,161–164] The reaction of planar triangular-shaped metalloligand $[Ru(phenba)_3]^{2+}$ and $Co(NO_3)_2$ generated a 2D network, however its reaction with $Eu(NO_3)_3$ produced **[Ru(phenba)$_3$+Eu$_2$]-MOF** with a 3D porous network, which efficiently promoted the selective transformation of CO_2 to HCOOH.[137] Under visible-light irradiation, $(Eu^{3+})_2$-SBU obtained two electrons from the excited $\{[Ru(phenba)_3]^{2+}\}^*$ units and was reduced to $(Eu^{2+})_2$, enabling the selective reduction of CO_2 to HCOOH *via* a two-electron process. In **[Ru(bpy)$_2$(dcbpy)+Ln]-MOFs** and **[Ir(ppy)$_2$(dcbpy)+Ln]-MOFs** (Ln = Yb, Er, Nd, Gd, Yb, Dy),[54,99,164] the photosensitizer groups acted as a good light-harvesting antenna to effectively sensitize Ln ions by d → f energy transfer, and achieving near-infrared luminescence. In addition, **[Ru(dcbpy)$_3$+La$_{1.75}$]-MOF** was constructed by the reaction of $[Ru(H_2dcbpy)_3]^{2+}$ with $LaCl_3$ in a molar ratio of 4 : 7. Water adsorption/desorption of **[Ru(dcbpy)$_3$+La$_{1.75}$]-MOF** triggered a reversible structural transformation, accompanying great influence on its ^{3}MLCT emission energy and ion conductivity. Vapochromic luminescence occurred *via* water vapor adsorption–desorption, in addition, the increased ion conductivity rate was proportional to humidity.[163] In isostructural complexes of **[Ru(dcbpy)$_3$+Ce$_{1.75}$]-MOF** and **[Ru(dcbpy)$_3$+Nd$_{1.75}$]-MOF**, different Ln ions have a great influence on their properties. MOFs synthesized with larger Ln ions could recover the ion conduction activation energy and the original porous structure at lower relative humidities.[162] Similarly, in **[RuH$_{5.5}$(dpbpy)$_3$+La$_{1.5}$]-MOF** (H_4dpbpy = 2,2′-bipyridine-4,4′-bis(phosphonic acid)) and **[RuH$_{5.5}$(dpbpy)$_3$+Pr$_{1.5}$]-MOF**, the ^{3}MLCT emission exhibited a blue-shift following the decreased humidity and red-shift with increased humidity, because water-adsorption triggered proton release and reconstruction of the porous structure. The proton conductivity of **[RuH$_{5.5}$(dpbpy)$_3$+La$_{1.5}$]-MOF** was much higher than **[Ru(dcbpy)$_3$+La$_{1.75}$]-MOF** due to the higher acidity of the phosphonic acid groups.[161]

Ln(III) ions have a high coordination number, and the combination of multifunctional carboxylate linker and Ln(III) ions can also form Ln$_6$-MOFs. Like **[Ru(Ir)+Zr$_6$]-MOFs**, the construction of **[Ru(Ir)+Ln$_6$]-MOFs** should also simultaneously use both metalloligands and its isometric dicarboxylate ligand when the metalloligands have no sufficient length. **Cu@[Ru(bpy)$_2$(bpydc)/bpydc+Eu$_6$]-MOF** was constructed by mixed use of $[Ru(bpy)_2(H_2bpydc)]^{2+}$, H_2bpydc, and [Cu(H_2bpydc)]Cl_2, which photocatalyzed the selective transformation of CO_2 to HCOOH with a high conversion rate (Fig. 9).[165]

PSM is another effective method to fabricate multinuclear Ru(N^N)$_3$ or Ir(C^N)$_2$(X^N) functionalized Ln-MOFs. Ce$_6$-MOLs. The combination of H_3BTB (H_3BTB = 1,3,5-benzenetribenzoate) and the photosensitive $[Ir(ppy)_2(HMBA)]^+$ (HMBA = 2-[5′-methyl-(2,2′-bipyridin)-5-yl]acetate) or $[Ru(bpy)_2(HMBA)]^{2+}$ group was introduced into the framework *via* the coordination with the Ce$_6$ cluster. **Ir(ppy)$_2$(MBA)@(BTB+Ce$_6$)-MOL** and **Ru(bpy)$_2$(MBA)@(BTB+Ce$_6$)-MOL** showed good photocatalytic HER performance due to the synergistic effect of photosensitizer and Ce$_6$ center (Fig. 10).[37] **Ru(bpy)$_2$(bpydc)@(bpydc+Ln$_6$)-MOFs** (Ln = Tb, Gd, Eu) were synthesized *via* the coordination linkage of Ru(N^N)$_2$ and (N^N) groups of frameworks, exhibiting photocatalytic thioether oxidation with high sulfoxide selectivity under mild conditions.[142]

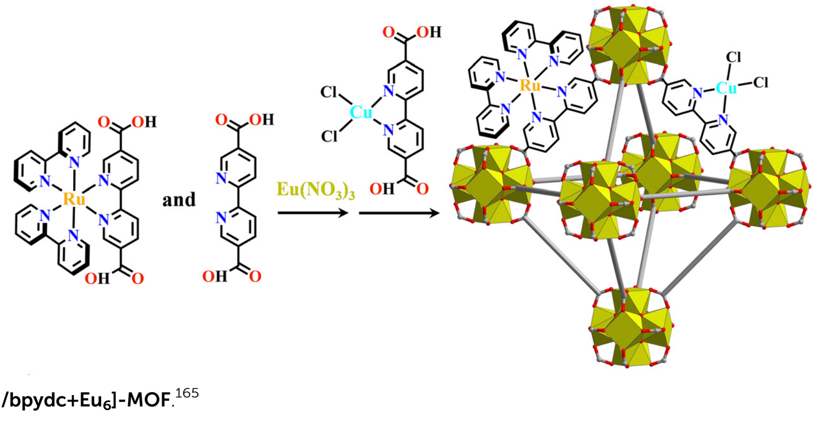

Fig. 9 **Cu@[Ru(bpy)$_2$(bpydc)/bpydc+Eu$_6$]-MOF**.[165]

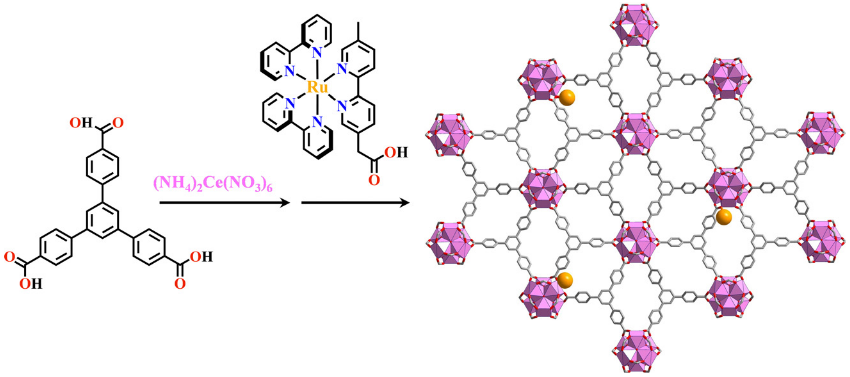

Fig. 10 **Ru(bpy)$_2$(MBA)@(BTB+Ce$_6$)-MOL**.[37]

The reaction of Ru(bpy)$_2$Cl$_2$ or Re(CO)$_3$Cl with (N^N)-sites of Al-MOF produced **[Re/Ru(bpy)$_2$(bpydc)]@(bpydc+Al)-MOF**, which showed high activity in photocatalytic CO$_2$ reduction under visible light.[166] The Al-OTf Lewis acid sites and Ir(ppy)$_2$(bpydc) photocatalytic sites were installed on Al-MOF. The obtained **[OTf/Ir(ppy)$_2$(bpydc)]@(bpydc+Al)-MOF** effectively catalysed the reductive cross-coupling to afford new aza arene derivatives. The close proximity of substrate binding centers and catalytic centers in the mesopore gave this heterogeneous catalyst better performance than the homogeneous counterpart. Furthermore, this MOF facilitated coupling reaction between the activated vinyl- or alkynyl-azaarenes and alkyl radicals.[167]

3. Ru(N^N)$_3$ or Ir(C^N)$_2$(X^N) functionalized COFs

A wide range of covalent organic frameworks (COFs) have been developed in the past two decades, because of their unique properties of good chemical and thermal stability, high specific surface area, and low skeletal density.[168] They have been widely employed in photocatalytic systems due to their chromophore and long-range π–π conjugated structure providing a platform for light-harvesting and efficient charge transfer.[108] Herein both crystalline COFs and amorphous COFs are described,[26] which are classified by the type of covalent bonds, topology, porosity and functions.[26]

3.1 Ru(N^N)$_3$ and Ir(C^N)$_2$(X^N) functionalized crystalline COFs

Similar to MOFs, COFs are also crystalline materials which have well-defined skeletons formed by the orderly and infinitely extended molecular tecons.[169] Different from MOFs, the covalent linkages give the whole framework with high conjugation and associated electronic properties.[170,171] Crystalline COFs are also more advantageous than amorphous species because crystalline networks possess well-ordered building units and better framework conjugation that is beneficial for the charge transport.[172] They exhibited numerous applications from drug delivery,[105,173,174] gas adsorption[175,176] and separation[177,178] to optoelectronics.[179] The introduction of the chelating coordination sites including N, O, and S elements into COFs makes them excellent metal catalyst supporters. The chelating sites could anchor the metal ions, permitting the uniform dispersion of metal catalysts into the supporters and preventing catalyst detachment. COFs can be easily functionalized to help the improvement of product selectivity. The high porosity and well-ordered pore channels of COFs accelerate the diffusion of substrates, and increase the approaching possibility between the substrates and catalytic center. These metal functionalized COFs have adjustable catalytic performances concerning high activity, product selectivity and reuse.

The construction of metal functionalized COFs also includes two main methodologies of metalloligand and PSM (Fig. 2).[113] The use of metalloligands is the most direct approach to fabricate metal-containing COFs with diverse topologies. For example, several interesting COFs were synthesized from metal–porphyrin[180–183] and glyoximate[184] precursors. PSM is another efficient approach to incorporate a metal catalyst into the frameworks *via* metal–ligand interactions, thus providing a reliable way to produce metal functionalized COFs for specific applications.[185] Although porous, the crystallinity and structure of COFs are maintained[186–190] by the PSM route, and an even distribution and precise location of the metal catalyst is difficult to achieve.

The condensation reaction of [Ru(bpy-OEt)$_3$]$^{2+}$ (bpy-OEt = 5,5′-bis(diethoxymethyl)-2,2′-bipyridine) metalloligands and multi-amine precursor including ETTA (ETTA = 4,4′,4″,4‴-(ethene-1,1,2,2-tetrayl)tetraaniline), TPB (TPB = 1,2,4,5-tetrakis-(4-aminolphenyl)benzene) or ETTBA (ETTBA = 4′,4‴,4′′′′′,4′′′′′′′-(ethene-1,1,2,2-tetrayl)tetrakis([1,1′-biphenyl]-4-amine)) produced three 3D *stp* topological networks **[Ru(bpy-OEt)$_3$+ETTA]-COF**, **[Ru(bpy-OEt)$_3$+TPB]-COF** and **[Ru(bpy-OEt)$_3$+ETTBA]-COF** (Fig. 11). Based on the photosensitive Ru(N^N)$_3$ unit, they possessed a strong light-harvesting ability and showed high photocatalytic activity in the HER process.[71] Most of the Ru(N^N)$_3$ or Ir(C^N)$_2$(X^N) functionalized COFs were assembled *via* PSM, and the (N^N)-unit of COFs was a commonly used bis-chelating group to grab metal catalysts.[187–189] For instance, Re(CO)$_3$Cl(N^N)-functionalized COFs efficiently reduced CO$_2$ to form CO under visible light illumination with high selectivity.[186] The reaction of

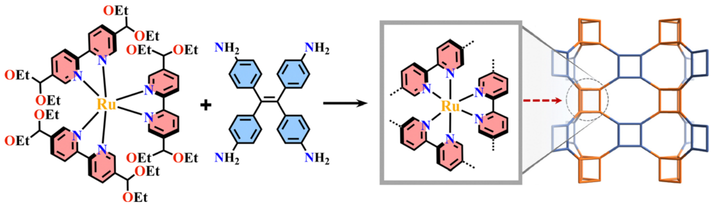

Fig. 11 3D **[Ru(bpy-OEt)$_3$+ETTA]-COF**.[71]

BPDCA (BPDCA = 2,2′-bipyridine-5,5′-dicarbaldehyde) and TAB (TAB = 1,3,5-tris-(4-aminophenyl) benzene) afforded an imine-linked 2D framework **(BPDCA+TAB)-COF** with an open (N^N)-site (Fig. 12), and its metalation with Ru(bpy)$_2$Cl$_2$ resulting in the formation of **Ru(N^N)$_3$@(BPDCA+TAB)-COF**. The site-specific functionalization of sp^3 C–H bonds of the C atom adjacent to a N atom is one less explored organic transformation. **Ru(N^Ru(N^N)$_3$@(BPDCA+TAB)-COF** photocatalyzed cross-dehydrogenative coupling between secondary amines and indoles with excellent yield.[116] Under visible light irradiation, the Ru(N^N)$_3$ moiety was excited into [Ru(N^N)$_3$]*, and it received one electron from the secondary amine offering a radical intermediate. The radical intermediate underwent deprotonation and formed a radical imine cation intermediate, and its quenching by indoles afforded the desired indolylglycine product. Another (N^N)-site-based 2D **(phendda+TAB)-COF** (phendda = 4,4′-(1,10-phenanthroline-3,8-diyl)dibenzaldehyde) was synthesized from TAB and phenanthroline-containing linear dialdehyde. The respective immobilization of [Ir(dFCFppy)$_2$Cl]$_2$ and Ni^{2+} into the porous framework led to **[Ni/Ir(dFCFppy)$_2$(N^N)]@(phendda+TAB)-COF**, enabling heterogeneous photocatalysis of C–C cross-couplings.[115] A similar complex, **[Ni/Ir(C^N)$_2$(N^N)]@(Tp+abpy)-COF** (Tp = 1,3,5-triformylphloroglucinol; abpy = 5,5′-diamino-2,2′-bipyridine) exhibited good performance in photocatalyzing C–N cross-coupling reactions with broad substrate diversity and high recyclability (Fig. 13).[117]

The reaction of TAPM (TAPM = tetra(*p*-aminophenyl)methane) and BPDCA produced a 3D diamondoid network **(BPDCA+TAPM)-COF** with 9-fold interpenetration, and its coordination with Ru(bpy)$_2$Cl$_2$ enabled visible light mediated cross-dehydrogenative coupling of tertiary amines and indoles under mild conditions (Fig. 14).[191]

Via host–guest interactions, the Ru(N^N)$_3$ or Ir(C^N)$_2$(X^N) derivatives could be incorporated into the pores of COFs,[105] yielding PS$\subset$COFs with diverse photocatalytic properties. The combined use of hydrazone-based COF photosensitizer and [Ir(terpyridine)(ppy)Cl]$^+$ catalyst exhibited efficient and durable photocatalytic CO$_2$RR. The reactivity and durability were highly improved compared with the bare [Ir(terpyridine)(ppy)Cl]$^+$, because the pore confinement effect from the COF facilitated the dispersion and weakened the aggregation of the Ir-catalyst.[108]

3.2 Ru(N^N)$_3$ and Ir(C^N)$_2$(X^N) functionalized amorphous COFs

The covalent bond strength determines the reversibility of the bond and crystallization of the COFs, thus imine-based COFs are readily formed with good crystallinity, while C–C bond-based COFs are extremely difficult to produce with crystalline networks. Amorphous COFs have disordered arrangement of building units and less porosity, but they commonly have

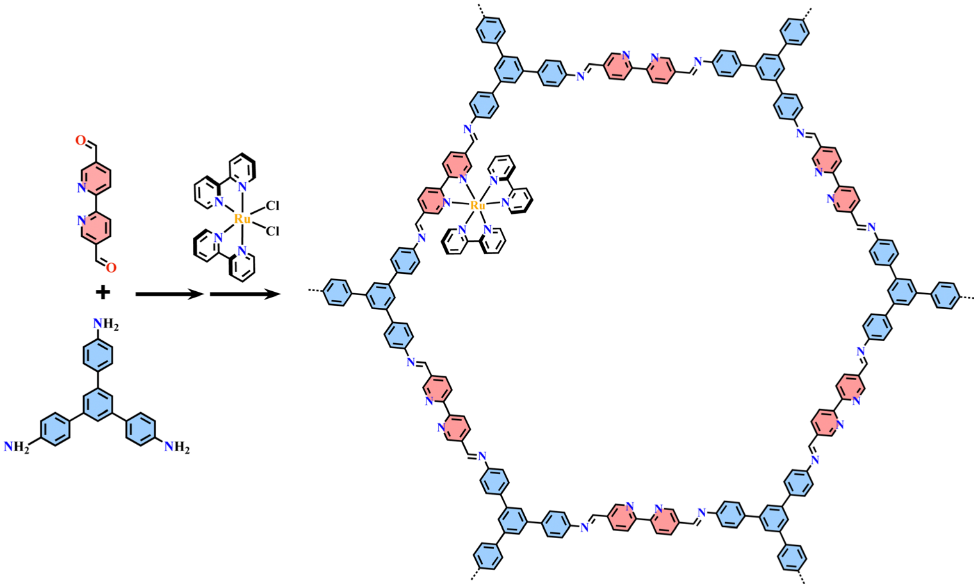

Fig. 12 2D **Ru(N^N)$_3$@(BPDCA+TAB)-COF**.[116]

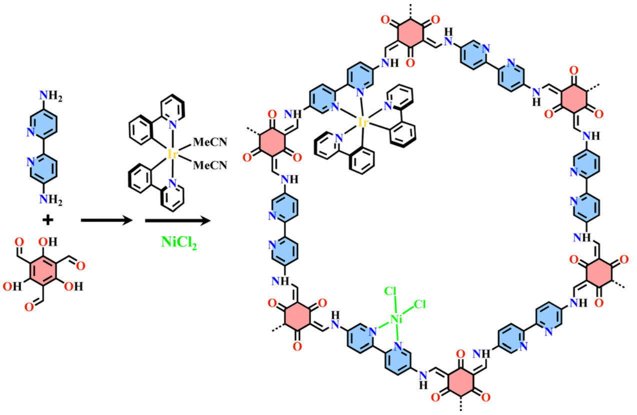

Fig. 13 2D **[Ni/Ir(C^N)$_2$(N^N)]@(Tp+abpy)-COF**.[117]

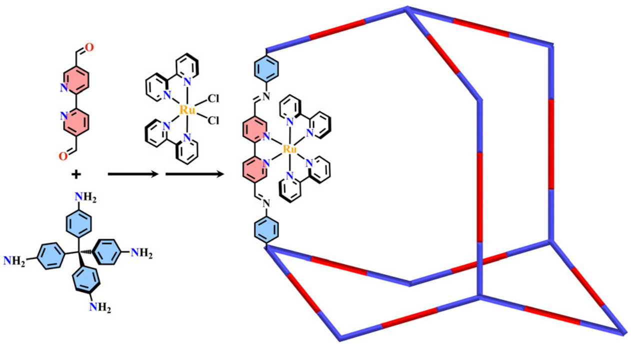

Fig. 14 3D **Ru(N^N)$_3$@(BPDCA+TAPM)-COF**.[191]

strong chemical stability and are emerging as versatile platforms for exploring new functional materials.[192–194] These cross-linked amorphous COFs are usually formed with inert covalent bonds through Suzuki reactions, alkyne trimerization reactions and oxidative coupling reactions, thus have high chemical stability. Amorphous COFs are not readily decomposed even under harsh reaction conditions,[195–198] but with less skeleton conjugation and a low surface area.

Heterogeneous photocatalysts can be formed by the incorporation of a photoredox catalyst into stable COF with excellent catalytic efficiency and easy separation from the reaction system.[199] A series of amorphous **[Ru(N^N)$_3$+TPMB]-COF** (TPMB = tetrakisphenylmethane borate) were synthesized from Pd-catalysed coupling reactions between one TPMB and two Br-Ru(N^N)$_3$-derivatives, and they showed visible-light driven photocatalytic activity in enantioselective alkylation of aldehydes.[199] The Suzuki coupling reaction of linear ditopic Ir(C^N)$_2$(tbubpy)-linker (tbubpy = 4,4′-di(*tert*-butyl)-2,2′-bipyridine) and TPMB afforded diamond type **[Ir(C^N)$_2$(tbubpy)+TPMB]-COF**, exhibiting good photocatalytic performance in a wide range of organic reactions, including aerobic oxidations of sulfides and oxidative hydroxylation of arylboronic acids, desulfurative conjugate addition to Michael acceptors, and Smiles-Truce rearrangement of alkyliodides (Fig. 15).[52] Their photocatalytic efficiency is better than the homogeneous prototype Ir(III) complexes owing to the porous structure and conjugated backbone of COFs. The cross-coupling of **[Ru(Ir)+TEPM]-COF** (TEPM = tetra(4-ethynylphenyl)methane) was obtained *via* Co$_2$(CO)$_8$-catalysed alkyne trimerization reactions of TEPM and Ru(N^N)$_3$ or Ir(C^N)$_2$(N^N)-based linear alkyne-linker. **[Ru(N^N)$_3$+TEPM]-COF** and **[Ir(C^N)$_2$(N^N) + TEPM]-COF** were highly effective in a variety of important organic transformations, such as aza-Henry reactions, α-arylation of bromomalonate, and oxyamination of an aldehyde.[200] FeCl$_3$-promoted oxidative coupling reaction of carbazole derivatives was an efficient methodology for the construction of organic polymers, and the self-polymerization of Ir(C^N)$_3$-carbazole derivatives produced **[Ir(C^N)$_3$+carbazole]-COF**, showing intense phosphorescence and high activity in photocatalytic aza-Henry reactions.[168] The Ir(C^N)$_2$(N^N) analogue **[Ir(C^N)$_2$(N^N)+carbazole]-COF** also showed good performance in aerobic photooxidation, such as sulfide oxidation, oxidative hydroxylation of arylboronic acids and cross-dehydrogenative coupling reactions.[201] The self-polymerization of 4,4′-di(4-vinylphenyl)-2,2′-bipyridine led to 1D polymer with open (N^N)-sites, and its bondage with Ru(bpy)$_2$Cl$_2$ or [Ir(ppy)$_2$Cl]$_2$ produced **Ru(N^N)$_3$-** or **Ir(C^N)$_2$(N^N)@polyethylene-COF** with an electrochemiluminescence response to tri-*n*-propylamine.[202]

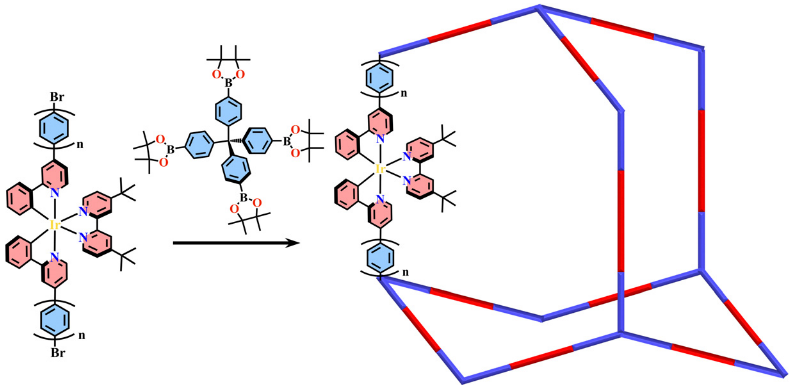

Fig. 15 Diamond type **[Ir(C^N)$_2$(tbubpy)+TPMB]-COF**.[52]

4. Ru(N^N)$_3$ or Ir(C^N)$_2$(X^N) functionalized metallasupramolecules

Different from the polymeric networks of MOFs, COFs[167] and SOFs, metallasupramolecules are discrete architectures with sufficient solubility in solvents, that exhibit unique properties in solution, such as host–guest and liquid luminescence.[203,204] Like the synthesis of MOFs, the construction of metallasupramolecules is also based on the coordination-driven assembly of metal ions and ligands. However, the structures of target architectures are commonly precisely foreseen *via* the controlled combination of metal ions and organic linkers.[203,205,206] The fruitful function and abundant structural configurations of these metallasupramolecules could be achieved by rational selection of well-designed ligands and metal precursors. The use of metalloligands with predesigned symmetry and configuration could contribute to the precise control of the architecture's geometry and their functionality could also be transferred to the metallasupramolecules.[207]

4.1 Ir(C^N)$_2$(N^N)-based metallasupramolecules

Similar to Pd(ethylenediamine) and *cis*-Pt(triethylphosphine)$_2$[208,209] groups, [Ir(ppy)$_2$Cl]$_2$ could also be utilized as a metal-corner with two available coordination sites and the ppy ligands are arranged in *C*,*C*-*cis*-*N*,*N*-*trans* orientation, which would sufficiently facilitate the self-assembly of Ir(C^N)$_2$(N^N)-based metallasupramolecules.[210] The combination of [Ir(ppy)$_2$Cl]$_2$-precursor and tritopic 1,3,5-tricyanobenzene produced octahedral metallasupramolecule **[Ir$_6$(1,3,5-tricyanobenzene)$_4$]**, and compared to the mononuclear complex, the incorporation of the Ir(C^N)$_2$(N^N) unit into the multimetallic array led to a significant luminescence enhancement (Fig. 16).[211] Two homochiral **[Ir$_3$(tpmc)$_2$]** metallo-cryptophane cages (tpmc = tris(4-pyridyl-methyl)-cyclotriguaiacylene) were synthesized from the assembly of cyclotriveratrylene-based chiral tripodal ligand and [Ir(ppy)$_2$Cl]$_2$-precursor. Interestingly, homochiral self-sorting of both the metal-corner and ligand occurred simultaneously, which was accelerated by the addition of a chiral guest (Fig. 17).[56] A similar **[Ir$_3$(ttpadtc)$_2$]** complex (ttpadtc = 2,7,12-trimethoxy-3,8,13-tris(4,4′-pyridyl-azophenylcarboxy)-10,15-dihydro-5*H*-tribenzo[*a*,*d*,*g*] cyclononane) was synthesized from the azobenzene-functionalized tripodal cyclotriguaiacylene derivative, showing reversible photo-isomerisation under blue light irradiation.[212]

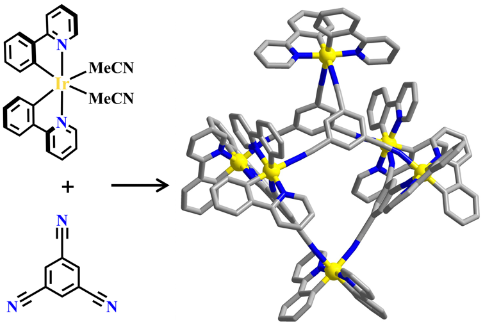

Fig. 16 Ir(C^N)$_2$(N^N)-based octahedral cage **[Ir$_6$(1,3,5-tricyanobenzene)$_4$]**.[211]

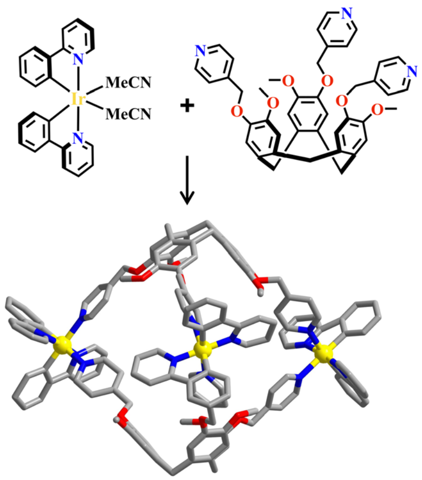

Fig. 17 Homochiral Ir(C^N)$_2$(N^N)-based cryptophane **[Ir$_3$(tpmc)$_2$]**.[56]

The reaction of [Ir(ppy)$_2$Cl]$_2$-precursor and ligands with both bis-chelating (N^N)-unit and *mono*-pyridyl units produced [Ir(mesppy)$_2$(qpy)]$^+$ (H-mesppy = 2-phenyl-4-mesitylpyridinato; qpy = 4,4′:2′,2″,4″,4‴-quaterpyridine) and [Ir(dFmesppy)$_2$(qpy)]$^+$ (H-dFmesppy = 2-(4,6-difluorophenyl)-4-mesitylpyridinato) metalloligands, and the assembly of them with Pd(MeCN)$_4$(BF$_4$)$_2$ (MeCN = acetonitrile) afforded homochiral hetero-metallacages **[Ir$_8$Pd$_4$]**. The blue-emitting [Ir(dFppy)$_2$(MeCN)$_2$]$^+$ ((H-dFppy = 2-(2,4-difluorophenyl)-4-phenyl)pyridine) guest was encapsulated into the cavity of **[Ir$_8$Pd$_4$]**, and energy transfer between the red-emitting **Δ-[Ir$_8$Pd$_4$]** cage and the guest molecules was observed (Fig. 18).[213] Another isostructural **[Ir$_8$Pd$_4$]** metallacage was constructed by [Ir(ppy)$_2$(qpy)]$^+$ and [Pd(MeCN)$_4$](BF$_4$)$_2$. Under visible light irradiation, the cubic barrel-shaped **[Ir$_8$Pd$_4$]** showed large $^1O_2$ quantum yields, which exhibited great potential in the photodynamic therapy and organelles-targeted cell imaging. The **[Ir$_8$Pd$_4$]** showed higher mitochondria-targeting efficiency and less dark toxicity compared with the [Ir(ppy)$_2$(qpy)]$^+$ metalloligand. The correlation coefficient of mitochondrial affected by the [Ir(ppy)$_2$(qpy)]$^+$ metalloligand was smaller than **[Ir$_8$Pd$_4$]**, which might be attributed to the higher positive charge of the metallacage.[58]

4.2 Ir(C^N)$_3$-based metallasupramolecules

Ir(C^N)$_3$-derivatives are widely used in light-emitting diodes because of their strong Φ_{PL} and large Stokes shift. The optical properties of Ir(C^N)$_3$-based materials involving phosphorescence lifetime and emission colour can be regulated *via* modification of conjugation, heteroatom type, and push–pull electron groups of ligands.[214,215] A triple helical organic cage was pre-organised with three (C–H^N)-units, and its cyclometallation with one Ir(III) ion formed a *fac*-Ir(C^N)$_3$ metallacage with a wide range of light emission and suffering from photoluminescence quenching in the presence of O$_2$ (Fig. 19).[216,217]

Like organic linkers, the metallotecons containing organic active groups, such as amino and aldehyde groups could

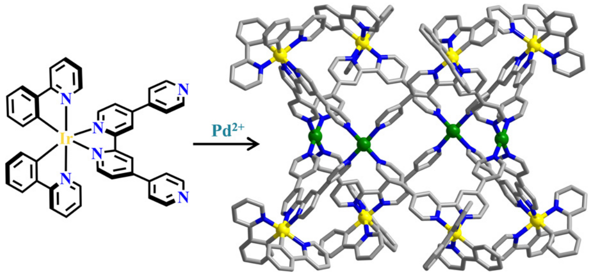

Fig. 18 Ir(ppy)$_2$(qpy)-based polyhedral cage **[Ir$_8$Pd$_4$]**.[213]

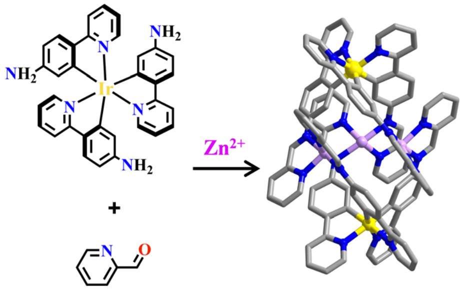

Fig. 20 Ir(appy)$_3$-based heterometallic polyhedron **[Ir$_2$Zn$_3$]**.[36]

further react with organic precursors. The reaction of metallotecon *fac*-tris-Ir(appy)$_3$ (H-appy = 4-(2-pyridinyl)phenylamine), 2-formylpyridine and Zn(BF$_4$)$_2$ afforded **[Ir$_2$Zn$_3$]** with the properties of photoluminescence, CO$_2$ fixation and nitrite separation (Fig. 20).[36] The isostructural complex **[Ir$_2$Co$_3$]** contained both a photosensitizer and Lewis catalytic center. Co^{2+} active sites were all in an open environment for favouring substrate bonding. **[Ir$_2$Co$_3$]** worked as a typical dual catalyst that synergistically combined photo-redox catalysis and metal coordination activation for a trichloromethylation of 2-acylpyridines with BrCCl$_3$.[65] In **[Ir$_2$Zn$_3$]** and **[Ir$_2$Co$_3$]** cages, the *fac* conformation of the Ir(C^N)$_3$ moiety constrained the geometry of Zn^{2+} and Co^{2+} with four N donors positioned in a controllable fashion.

4.3 Ru(N^N)$_3$-based metallasupramolecules

Ru(N^N)$_3$ is one type of renowned photosensitizer[218] with intriguing photochemical applications in light-harvesting and photocatalysis.[46] Ru(N^N)$_3$ derivatives have a moderate redox state,[6] and they have been widely employed in various types of photocatalytic reactions.[219–222] As stable and functional building blocks, Ru(N^N)$_3$ units are also used in the construction of interesting metallasupramolecules.[223–227]

[Pd$_6$Ru$_8$] metallacages attached with a Ru(N^N)$_3$-unit were synthesized from the reaction of bulky triangular [Ru(piphen)$_3$]$^{2+}$-metalloligand (piphen, 2-(pyridin-3-yl)-1*H*-imidazo[4,5-*f*][1,10]phenanthroline) and Pd(MeCN)$_4$(BF$_4$)$_2$, and these metallacages featured a quite high Φ_{PL}.[39] The **[Pd$_6$Ru$_8$]** cage (Fig. 21) has a rhombododecahedral shape with a 5350 Å^3 cavity and 12 open windows. The large hydrophobic size-selective cavity facilitated effective trapping of a nonpolar and water-immiscible aromatics guest in a water-containing hydrophilic solvent. The ^{1}H NMR study of guest inclusion confirmed the formation of noticeable interactions between hosts and guests due to the encapsulation of aromatic guests, which was expected to form facile π–π interactions with the phenanthroline moieties, thus **[Pd$_6$Ru$_8$]** had potential applications in drug delivery. In addition, inclusion tests on photosensitive guest molecules against UV light radiation confirmed that the cage offered better photoprotection than the pure [Ru(piphen)$_3$]$^{2+}$-metalloligand, suggesting that the **[Pd$_6$Ru$_8$]** metallacage could well shield the guests to prevent undesired photolysis.[228] Furthermore, the **[Pd$_6$Ru$_8$]** cage was incorporated with multiple photo- and Lewis acid centers,[229] in which the Ru(N^N)$_3$-unit acted as a photosensitizer and Pd^{2+} as the catalyst. Electron transfer from the [Ru(piphen)$_3$]$^{2+}$ photoactive center to the Pd^{2+} center resulted in intramolecular charge separation, and they worked synergistically for the efficient photocatalyzed HER. In the host–guest system, TTF (TTF = tetrathiafulvalene) guests acted as an electron relay mediator to improve the overall electron transfer efficiency by virtue of redox-guest modulation of the photo-induced electron transfer process. In this process, TTF strongly quenched **[Pd$_6$Ru$_8$]** emission due to the formation of a host–guest adduct. In contrast, without host–guest interactions, TTF-derivatives slightly influenced the emission quenching of **[Pd$_6$Ru$_8$]** and H$_2$ evolution. This host–guest interaction between redox-active metallacages and a guest provided a model to understand and optimize redox events, such as photocatalytic activities in a confined nanosapce.[230] The homochiral Δ/Λ-[Ru(piphen)$_3$]$^{2+}$-metalloligand led to the formation of homochiral **[Pd$_6$Ru$_8$]** (**Δ-[Pd$_6$Ru$_8$]** and **Λ-[Pd$_6$Ru$_8$]**) featured with large D_4-symmetric chiral space, which was imposed by the predetermined [Ru(piphen)$_3$]$^{2+}$-octahedral stereo configuration. They had an enantio-separation ability

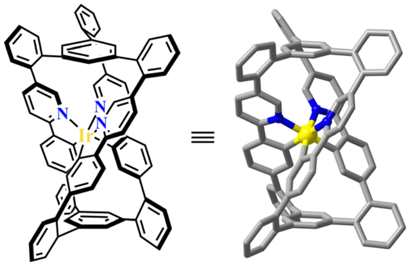

Fig. 19 *Fac*-Ir(C^N)$_3$-based triple helical architecture.[217]

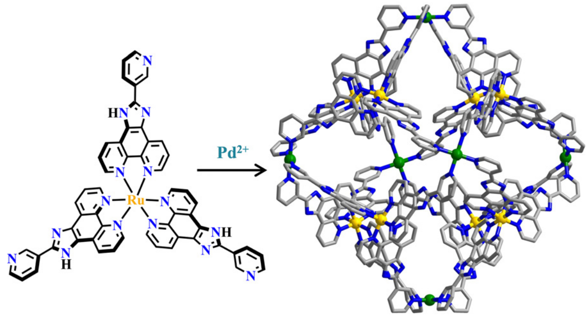

Fig. 21 Ru(piphen)$_3$-based **[Pd$_6$Ru$_8$]**.[228]

for atropisomeric compounds with C_2 symmetry, thus recognizing *R*- and *S*-BINOL (BINOL = 1,1′-bis(2-naphthol)) enantiomeric guests in solution.[60] The homochiral metallasupramolecules possessed dual functionality of photoredox reactivity and stereoselectivity. Naphthol guests were encapsulated into the racemic or enantiopure cages, then underwent a regiospecific 1,4-coupling rather than the normal 1,1-coupling and formed 4-(2-hydroxy-1-naphthyl)-1,2-napthoquinones. This photoinduced regio- and enantioselective coupling was achieved in the confined chiral space of homochiral **[Pd_6Ru_8]**. Under aerobic conditions, the photo-excited $[Ru(piphen)_3]^{2+}$ centers were quenched by O_2, affording hydrogen peroxide (H_2O_2) and hydroxyl radical ($^{\bullet}OH$). The naphthol substrates were oxidized by **[Pd_6Ru_8]**$^{+}$ *via* single-electron-transfer to give radical species, and its further reaction with $^{\bullet}OH$ produced intermediate naphthalene-1,2-dione. Through regioselective 1,4-coupling, 4-(2-hydroxy-1-naphthyl)-1,2-napthoquinone was exclusively obtained.[231] By virtue of the molecular cage confinement effect and multi-functions coupling synergism, racemic **[Pd_6Ru_8]** accelerated [2+2] photodimerization of symmetric acenaphthylene with seteroselectivity and formed anti-products. Homochiral **Δ-** or **Λ-[Pd_6Ru_8]** photocatalyzed dimerization of 1-Br-acenaphthylene offered the corresponding (6*bS*,6*cS*,12*bR*,12*cR*)-6*b*,6*c*-dibromo-6*b*,6*c*,12*b*,12*c*-tetrahydrocyclobuta [1,2-*a*:3,4-*a*′]diacenaphthylene or (6*bR*,6*cR*,12*bS*,12*cS*)-6*b*,6*c*-dibromo-6*b*,6*c*,12*b*,12*c*-tetrahydrocyclobuta [1,2-*a*:3,4-*a*′] diacenaphthylene, respectively.[232] Synergistic actions arising from imidazole-N coordination, imidazole-N protonation-deprotonation of **[Pd_6Ru_8]**, cage hydrophobicity, and host–guest electrostatic interactions facilitated carbanionic intermediate stabilization of terminal alkynes and C–H activation to achieve Glaser-coupling and unusual H/D-exchange. The immiscible mixture of alkynes and **[Pd_6Ru_8]** in aqueous solution turned into a homogeneous phase rapidly, clearly owing to the inclusion of alkynes by the hydrophobicity of the cage *via* a phase transfer process. This provided a useful catalytic method combining advantages from heterogeneous, homogeneous, and phase transfer to enzymatic catalysis.[233]

A $Ru(bpy)_2Cl_2$ fragment was used as a 90° acceptor tecton, and the Cl^- sites of *cis*-$Ru(bpy)_2Cl_2$ could be occupied by pyridine of the pyridyl linker, producing a **[Ru_4(4,4′-bipyridine)$_4$]** molecular square or **[Ru_6(TPT)$_4$]** (TPT = 2,4,6-tri(pyridin-4-yl)-1,3,5-triazine) truncated tetrahedral cage respectively. The **[Ru_6(TPT)$_4$]** cage possessed emergent properties attributed to its unique electronic structure, resulting in increased visible-light absorption and biexponential decay of an emission band.[53] A heteronuclear metallacage **[Pd_4Ru_8]** was assembled by $[Ru(tbubpy)_2(qpy)]^{2+}$-metalloligand and $Pd(MeCN)_4(BF_4)_2$ with high Φ_{PL}.[234]

5. Ru(N^N)$_3$ or Ir(C^N)$_2$(X^N) functionalized organic supramolecules

Supramolecular architectures could be classified into metallasupramolecules and organic supramolecules. Metallasupramolecules are constructed by the metal–ligand interactions, and organic supramolecules are assembled *via* covalent linkages.[19] The Ru(N^N)$_3$ or Ir(C^N)$_2$(X^N) functionalized organic supramolecules are described here. Luminescent tetrahedral molecular cages **[Ru(phen)$_2$(N^N)+tris(2-aminoethyl)amine]** were formed *via* the reaction of linear precursor {Ru(phen)$_2$[(3,3′:6′,2″:5″,3‴-quaterpyridine)-6,6‴-dicarbaldehyde]}$^{2+}$ with tris(2-aminoethyl) amine and Zn{*bis*(trifluoromethanesulfonyl)imide}$_2$. The stereoisomeric chirality of the Ru(N^N)$_3$-center was passed to the synthesized cage (Fig. 22).[46]

Mitochondria DNA-targeted photodynamic therapy was used for cancer treatment with a series of **[*fac*-Ir(ppy-CHO)$_3$+diamine]** metallohelices (H-ppy-CHO = 4-(2-Pyridyl) benzaldehyde). Aldehyde groups of ***fac*-Ir(ppy-CHO)$_3$** were helically arranged around the Ir(III) center with a facial propeller-like configuration. Connecting the preorganized Δ/Λ-*fac*-Ir(ppy-CHO)$_3$ modules with different diamines by dynamic imine-coupling chemistry allowed for the formation of **[*fac*-Ir(ppy-CHO)$_3$+diamine]** metallohelices with stereochemical information and suitable size. The odd-even character and length of the diamine alkyl linkers determined the conformations of two Ir(III) centers of one metallohelices with the same chirality or heterochirality (Fig. 23). The high degree of narcissistic chiral self-sorting occurred during the condensation, and a pair of enantiomers were obtained even when diamines with an even number of C atoms were introduced. For an odd number C-based diamine, only one achiral cage was obtained with two heterochiral Ir(III) centers. To improve their stabilities for biological applications, these imine-linked **[*fac*-Ir(ppy-CHO)$_3$+diamine]** metallahelices were further reduced into amine-inked metallohelices by $NaBH_4$. Notably, in sharp contrast to the corresponding imine complex, the Φ_{PL} and $^1O_2$ quantum yields of these amine-linked metallohelices were significantly enhanced. DNA-binding affinities influenced the photodynamic therapy treatment. 1,5-Pentanediamine had an appropriatelength between diamine spacers, thus showed stronger DNA-binding affinities in a minor groove manner with high photodynamic therapy efficacy.[32] Employing Δ/Λ-*fac*-Ir(ppy-CHO)$_3$ modules with chiral *RR*/*SS*-*trans*-1,2-diaminecyclohexane spacers, homochiral dinuclear **Δ*R*-[*fac*-Ir(ppy-CHO)$_3$+cyclohexylamine]** and **Λ*S*-[*fac*-Ir(ppy-CHO)$_3$+cyclohexylamine]** were obtained. Their chiral porous crystals could be used for the effective enantioseparation of atropisomers, yielding

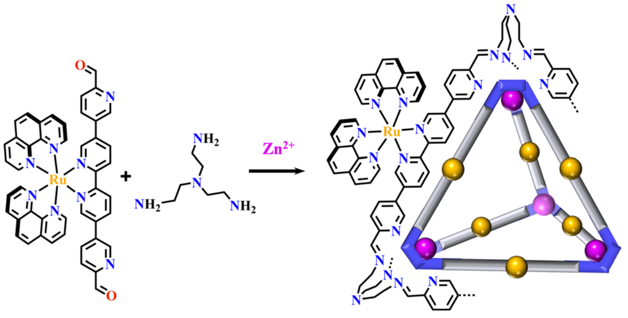

Fig. 22 Luminescent tetrahedral cage **[Ru(phen)$_2$(N^N)+tris(2-aminoethyl)amine]**.[46]

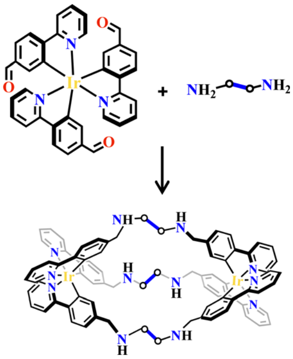

Fig. 23 **[*fac*-Ir(ppy-CHO)$_3$+diamine]**-helicates.[32]

$>$99% ee for BINOL in a single separation cycle. These molecular crystals maintained consistent ee values even after 10 cycles of enantioseparation. Changing the helicands as achiral ethylenediamine, the resulting crystalline homochiral helicates **Δ-[*fac*-Ir(ppy-CHO)$_3$+cyclohexylamine]** and **Λ-[*fac*-Ir(ppy-CHO)$_3$+cyclohexylamine]** showed no enantioselectivity despite displaying a similar adsorption capacity. The strict chirality matching between the extrinsic 3D chiral channels and the enantiopure guests may dominate the enantioseparation process.[64]

A chiral Ir(C^N)$_2$(N^N)-based building block was regionally coordinated to a bipyridyl-based strand, which subsequently extended into a chiral building block with six vacant pyridine-based chelating sites, and the building block was dimerized through coordination with four Zn(OTf)$_2$ and formed a Ir(C^N)$_2$(N^N)-based closed-loop helicate (Fig. 24). Helicate crossing was captured covalently by ring closing metathesis of pendant alkenes and a topological chiral star of David catenane was formed, where the Zn^{2+} could be removed with the maintenance of an interlocked structure. The kinetic stability of the coordinated Ir(III) center ensured that the circular helicate was formed as a single enantiomer. In the star of **David [2] catenane**, both complexes with and without coordinated Zn^{2+} ions retained the photophysical characteristic of the Ir(C^N)$_2$(N^N) unit.[67]

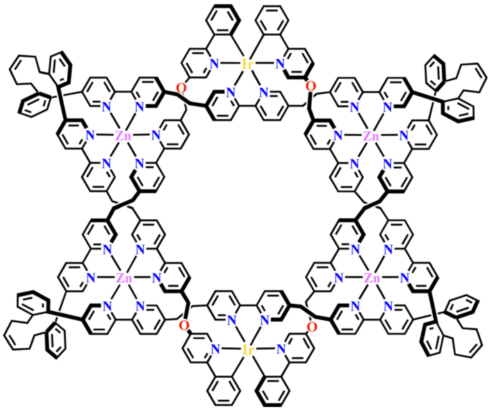

Fig. 24 Ir(C^N)$_2$(N^N)-based triply interlocked star.[67]

6. Ru(N^N)$_3$ and Ir(C^N)$_2$(X^N) functionalized SOFs

SOFs are crystalline, ordered supramolecular polymers with defined structures. Many reaction conditions including solvents, temperature, pH and reaction time could have a great influence on the synthesis of MOFs and COFs, however the construction of SOFs depends on the mild formation of intermolecular interactions,[235] including hydrogen bonds, electrostatic, and π–π interactions, *etc.*[235]

Using photosensitized building blocks, the homogeneity permitted SOFs with maximum visible light radiation.[104] *Via* host–guest interaction, the combination of six-armed Ru(N^N)$_3$-based precursors with cucurbit[8]uril generated a **{Ru(N^N)$_3$+cucurbit[8]}-SOF** at room temperature, which maintains its solid-state structure in solution, achieving the encapsulation of {P$_2$W$_{18}$} in a one-cage-one-guest manner. This material realized homogeneous catalytic H$_2$ production under visible light irradiation with high efficiency (Fig. 25).[70] Another similar cubic **{Ru(N^N)$_3$+cucurbit[8]}-SOF** was obtained from the reaction of [Ru(bpy)$_3$]$^{2+}$-based acyl hydrazine with aldehyde in the presence of cucurbit[8]uril. The remarkable size could adsorb discrete anionic {P$_2$W$_{18}$} through electrostatic interaction, which was further stabilized in the cationic framework. The corresponding SOF remarkably facilitated visible light-induced electron transfer from Ru(N^N)$_3$ units to POM guests, enabling highly efficient photocatalytic H$_2$ production.[69]

In addition, Ru(bpy)$_2$(dcbpy) and [Ru(dcbpy)$_3$]$^{4-}$ photosensitizers, {P$_2$W$_{18}$} and {PW$_{12}$} POMs could also be encapsulated in the pores of SOFs as guests through host–guest interactions. The nanospace provided by SOFs simultaneously encapsulated Ru(N^N)$_3$-photosensitizer and POMs. The improvement of electron transfer between the Ru(N^N)$_3$-photosensitizer and POMs catalyst greatly improved the photocatalytic H$_2$ production.[104]

7. Photocatalysis investigation of Ru(N^N)$_3$ and Ir(C^N)$_2$(X^N) functionalized architectures

Ru(N^N)$_3$ and Ir(C^N)$_2$(X^N) derivatives are commonly employed as photocatalysts owing to their strong visible light absorption capability, long-lived photoexcited states, dually effective excited state oxidant and reductant. The light absorption range and redox potentials of three types of Ru(N^N)$_3$, Ir(C^N)$_2$(C^N) and Ir(C^N)$_3$ samples are quite different. As shown in Table 2,[81] photoexcited Ir(ppy)$_3$ has a stronger reduction capability than [Ru(bpy)$_3$]$^{2+}$ and [Ir(ppy)$_2$(bpy)]$^+$ owing to its lower redox potentials. For the same type of PS, the redox potential of [Ir(ppy)$_2$(bpy)]$^+$ is higher than [Ir(ppy)$_2$(tbubpy)]$^+$, but lower than [Ir(dFCFppy)$_2$(tbubpy)]$^+$, indicating the influence of the electron donating or withdrawing group of (N^N) on redox potential. Their photophysical properties could be finely regulated *via* the judicious choice of (N^N) or (X^N) ligands, providing a designable and flexible photocatalyst platform for specific reactions.

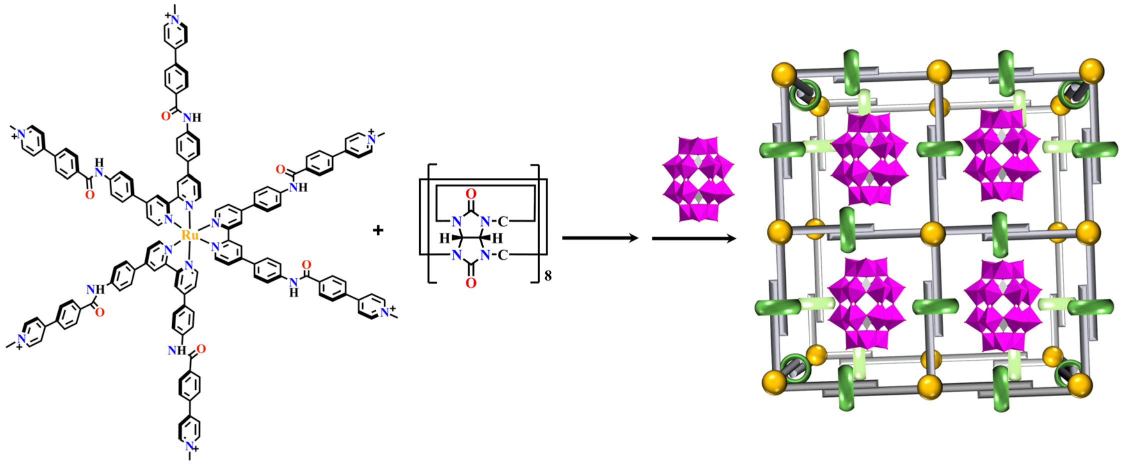

Fig. 25 $\{P_2W_{18}\}\subset\{$Ru(N^N)$_3$+cucurbit[8]$\}$-SOF.[70]

Table 2 Redox potentials $E_{1/2}$ (*V vs.* SCE) and selected photophysical properties of commonly utilized Ru(N^N)$_3$ and Ir(C^N)$_2$(X^N) photocatalysts[a][81]

Entry	Complex	Excitation λ_{max}/(nm)	Emission λ_{max}/(nm)	Excited-state lifetime t/(ns)	$E_{1/2}(M/M^-)$	$E_{1/2}(M^+/M^*)$	$E_{1/2}(M^*/M^-)$	$E_{1/2}(M^+/M)$
1	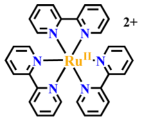	452	615	1100	−1.33	−0.81	+0.77	+1.29
2	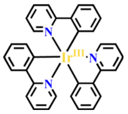	375	494[b]	1900	−2.19	−1.73	+0.31	+0.77
3	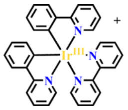	420	585	307	−1.42	−0.87	+0.70	+1.25
4	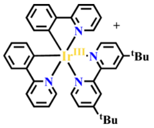	410	581	557	−1.51	−0.96	+0.66	+1.21
5	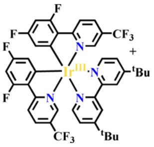	380	470	2300	−1.37	−0.89	+1.21	+1.69

SCE = standard calomel electrode. M represents the Ru(N^N)$_3$ or Ir(C^N)$_2$(X^N) complex. [a] Measurements were performed in MeCN at room temperature unless otherwise noted. [b] Determined in 1:1 CH_5OH/CH_3OH at 77 K.

Ru(N^N)$_3$ and Ir(C^N)$_2$(X^N) derivatives are good photosensitizers (PSs), and the combined use of the PS and Lewis acid catalyst (Cat) generated novel photocatalytic activities. For example, Ru(N^N)$_3$ derivatives are good PS for water splitting because of their appropriate redox ability. According to thermodynamic criteria, Ru(N^N)$_3$ catalysts can drive the photolysis of H_2O, but this is rarely observed due to the high reaction barriers. Only when Ru(N^N)$_3$ PS and other Cat are employed together, can the photocatalytic H_2O splitting be achieved. Ru(N^N)$_3$ or Ir(C^N)$_2$(X^N) based PS and Cat photocatalytic systems commonly follow the three-component system of ''PS-Cat-D/A'' (D = electron donor, A = electron acceptor). As shown in Fig. 26, PS* acts as a mediator and transfers an electron from the electron donor D to Cat, which involves two mechanisms of oxidative quenching and reductive quenching.[236] The oxidative quenching process involves single-electron-transfer from PS* to Cat, accompanied with the formation of high-oxidation-state PS^+ and reduced Cat^-. The PS^+ gets one electron from D to achieve recovery. The reduction quenching process involves PS* grabbing the electrons from D associated with the formation of reduced PS^- and single-electron-transfer occurs from PS^- to Cat. In a word, reductive refers to the reduction of PS*, whereas

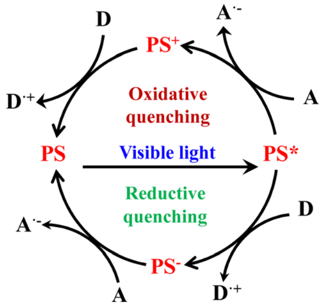

Fig. 26 Mechanisms of oxidative quenching and reductive quenching.[237]

the external D is oxidized in the same process. Oxidative means oxidation of the PS* concomitant with the reduction of Cat.[237] The incorporation of both PS and catalytic sites into a confined nanospace not only increases the apparent concentration of both PS and Cat[104] but also facilitates multielectron transfer to drive high photocatalytic performance, as well as stabilizing the PS and Cat *via* site isolation.[47,114,238–240] Many types of photocatalytic reactions have been achieved using the Ru(N^N)$_3$ or Ir(C^N)$_2$(X^N) functionalized architectures.

7.1 Photocatalytic hydrogen evolution reaction (HER)

Photocatalytic HER is an important approach to achieve solar-to-chemical energy conversion. The HER involves both oxidative quenching and reductive quenching mechanisms.[140,150] Reductive quenching-based photoreduction can take place when both requirements of $E(\mathrm{PS/PS^-}) < E(\mathrm{Cat/Cat^-}) < E(\mathrm{H^+/H_2})$ and $E(\mathrm{PS^*/PS^-}) > E(\mathrm{D^+/D})$ are met. Oxidative quenching-based photoreduction takes place when both requirements of $E(\mathrm{PS^+/PS^*}) < E(\mathrm{Cat/Cat^-}) < E(\mathrm{H^+/H_2})$ and $E(\mathrm{PS^+/PS}) > E(\mathrm{D^+/D})$ are satisfied. Different Ru(N^N)$_3$ and Ir(C^N)$_2$(X^N) PSs should be matched with the corresponding Cat to achieve the HER. For instance, when [Ir(ppy)$_2$(N^N)]$^+$ and [Ru(bpy)$_2$(N^N)]$^{2+}$ were used as photosensitizers and {Ni$_4$P$_2$}-based POMs as catalysts. [Ir(ppy)$_2$(N^N)]$^+$ drove a highly efficient HER process, but [Ru(bpy)$_2$(N^N)]$^{2+}$ was proved useless, because −0.70 eV of E{[Ir(ppy)$_2$(N^N)]$^{2+}$/([Ir(ppy)$_2$(N^N)]$^+$)*} was negative enough to permit electron accumulation at {Ni$_4$P$_2$} POMs, enabling {Ni$_4$P$_2$} to have enough reduction activity for H_2 production. In contrast, −0.62 eV of E{[Ru(bpy)$_2$(N^N)]$^{3+}$/([Ru(bpy)$_2$(N^N)]$^{2+}$)*} was higher than the −0.65 eV redox potential of {Ni$_4$P$_2$}, thus cannot give {Ni$_4$P$_2$} with a more negative reduction potential for driving H_2 production (Fig. 27).[150]

The incorporation of POMs into Ru(N^N)$_3$ and Ir(C^N)$_2$(X^N) functionalized architectures produced interesting photocatalytic activities arising from the synergistic effect of the photosensitizer, POMs and well-defined nanospace. In **{P$_2$W$_{18}$}⊂[Ru(bpy)$_2$(dbpydc)+Zr$_6$]-MOF**[114] and **{Ni$_4$P$_2$}⊂[Ru(bpy)$_2$(dbpydc)+Zr$_6$]-MOF**,[150] the POMs were encapsulated into the porous cavity of the photosensitizer-functionalized frameworks *via* electrostatic force and host–guest interaction, and the proximity of POMs to the photosensitizer allowed a facile multielectron transfer and enabled an efficient visible-light-driven HER with high turnover numbers. Photophysical and electrochemical studies proved that the oxidative quenching of PS* by POMs was the initiating step of the HER. The simultaneous encapsulation of Ru(N^N)$_3$ derivatives and POMs into a crystalline framework, producing an excellent photocatalyst for the HER. In these networks, the electron transition distance was shortened because the photosensitizer unit and POM catalyst were confined together *via* electrostatic force and host–guest interactions, leading to sharply increased photocatalytic activity in the HER process.

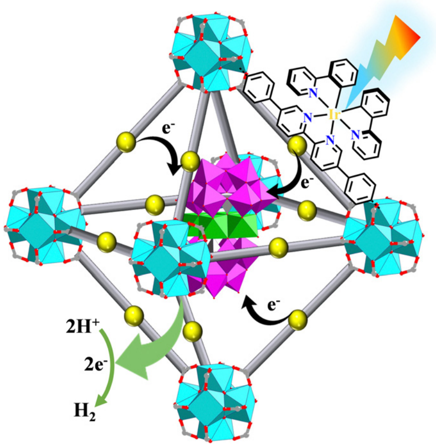

Fig. 27 HER process catalysed by **{Ni$_4$P$_2$}⊂[Ir(ppy)$_2$(dbpydc)+Zr$_6$]-MOF**.[150]

Apart from POMs, the metal cluster in SBUs can also act as a catalyst. In **[Ru(bpy)$_2$(bpydc)/bpdc+Ti$_3$]-MOF** and **[Ir(ppy)$_2$(bpydc)/bpdc+Ti$_3$]-MOF**, photophysical and electrochemical studies proved that the photocatalytic HER proceeded reductive quenching of PS* and then an electron was transferred from the reduced PS to Ti$_3$ SBUs. Density functional theory calculations revealed that key steps of the HER process included the Ti^{3+}-OH was protonated to generate the Ti^{3+} species with a vacant coordination site, and proton-coupled electron transfer to provide the key Ti^{4+}-H intermediate.[140] In **Ir(ppy)$_2$(MBA)@(BTB+Ce$_6$)-MOL** and **Ru(bpy)$_2$(MBA)@(BTB+Ce$_6$)-MOL**, the proximity of photosensitizing ligands and Ce$_6$-SBUs facilitated electron transfer to drive the photocatalytic HER under visible light. The PS* in the MOL was reductively quenched and then transferred electrons to Ce$_6$-SBUs to generate reduced Ce^{3+} centers, and they were photoexcited to Ce^{3+}* species for further HERs.[37]

In addition, the metal center anchored at the ligands can also be employed as a catalyst, and they were combined with a Ru(N^N)$_3$ or Ir(C^N)$_2$(X^N) photosensitizer for bifunctional catalysis. The incorporation of both photosensitizer and metal catalyst into one network, enabled the fast electron–hole separation and transfer to metal catalyst for excellent photocatalytic performance. The network of **[Ir(ppy)$_2$(bpydc)/bpydc+Zr$_6$]-MOF** had open (N^N)-sites that can capture K[PtCl$_3$(C$_2$H$_4$)]. The catalyst-incorporated framework not only promoted photoelectron transfer from the Ir(C^N)$_2$(X^N) photosensitizer to the Pt catalyst, but also increased the stability of the backbone.[47] The stable **Co@[Ru(bpy)$_2$(bpydc)/bpydc+Zr$_6$]-MOF** exhibited extra high photocatalytic activity for H_2 production with recycle and reuse performances. The rate-limiting step was the formation of Co^+ intermediate species reduced by a photoelectron.[241]

7.2 Photocatalytic CO_2 reduction reactions (CO_2RR)

The ever-increasing atmospheric CO_2 from fossil fuel consumption raises growing concerns about global warming.[242,243] Photocatalytic CO_2 transformation to other valued chemicals attracted great interest. However, selective CO_2 transformation remains a challenge as the existing catalyst usually has low catalytic efficiency and poor product selectivity and often suffers from the competing HER.[165,244]

In recent years, several Ru(N^N)$_3$ and Ir(C^N)$_2$(X^N) functionalized architectures have been employed in the CO_2RR process, in which Ru(N^N)$_3$ and Ir(C^N)$_2$(X^N) units are used as the photosensitizer, and metal clusters[137,151] or metal complexes are used as coordination catalytic centers, such as Cu,[138,165] Re, Mn,[155] Ni,[139] and Co.[149] The CO_2RR also obeys the three-component form of "PS-Cat-D" involving two mechanisms of oxidative quenching and reductive quenching. The electrons are transferred from PS* to Cat, and the photogenerated holes in PS* abstract the electrons from D.

CO_2 can be reduced to various products of CO, HCOOH, HCHO, CH_3OH, and CH_4 by gaining different numbers of electrons and protons.[244] During the CO_2RR, the light-excitation attributes, band structure, and separation efficiency of photogenerated charge carriers are three important factors to influence photocatalytic CO_2 transformation. Moreover, CO_2 adsorption/activation, catalytic active sites, and intermediate adsorption/desorption are also critical in regulating the product selectivity.[244] Redox potentials of photocatalytic CO_2 reduction to different products (Fig. 28) can theoretically control the product selectivity of CO_2 transformations. In addition, the C, H, and O affinity of the photocatalyst has a great influence on the adsorption and desorption of reactants/intermediates, the sequence of hydrogenation and deoxygenation reactions, reaction pathways and product selectivity.

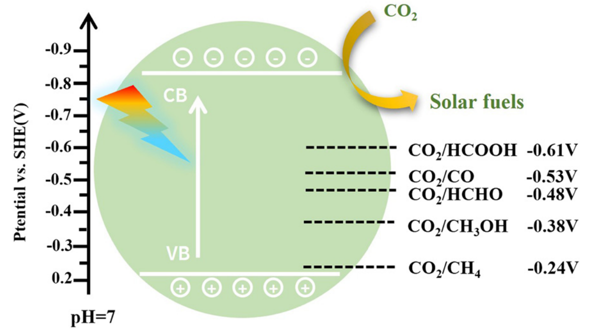

Fig. 28 Reduction potentials of various products for the CO_2RR (SHE = standard hydrogen electrode, CB = conduction band, VB = valence band).

Herein, we elaborate on the materials based on the types of products formed. HCOOH is one potential compound for fuel cells and hydrogen storage.[245,246] **[Ru(phenba)$_3$+Eu$_2$]-MOF** has Eu_2 clusters as connecting nodes and Ru(phenba)$_3$-metalloligand as linkers, which selectively reduced CO_2 to HCOOH in a two-electron process with an excellent rate. The efficient electron transfer from $[Ru(phenba)_3]^{2+}$-units to Eu_2 clusters allowed high HCOOH production rates. The (Eu–H_2O–Eu)-active sites not only accepted electrons but also captured CO_2, thus could achieve highly efficient transformation of CO_2 to HCOOH (Fig. 29).[137] **[Ru(cptpy)$_2$+Zr]-MOF** was composed of $[Ru(cptpy)_2]^{2+}$-metalloligand and ZrO_8 cluster and had both high chemical stability and photostability, and it efficiently photocatalyzed the reduction of CO_2 to HCOOH under visible light irradiation.[151] In addition, bimetallic catalysis can reduce CO_2 to HCOOH. Highly selective photoreduction of CO_2 to HCOOH was achieved with a high yield by hierarchical integration of $[Ru(bpy)_2(H_2bpydc)]^{2+}$ photosensitizer and monometallic Cu(bpydc)Cl$_2$ catalyst into a stable **Cu@[Ru(bpy)$_2$(bpydc)/bpydc+Eu$_6$]-MOF**.[165] The multinuclear complexes of **[Ru(N^N)$_3$]$_x${Ru(N^N)$_2$(CO)$_2$}$_y$** combined PS and Cat together *via* covalent linkage, exhibited high photocatalytic efficiency and HCOOH selectivity in CO_2 transformation. The ratio between PS and Cat strongly affected the photocatalytic activities, and the higher PS ratio gave a better yield of HCOOH. Weak conjugation of PS and Cat could be also beneficial for better photocatalytic performance.[247]

Among all the possible technological routes, visible-light-driven two-electron reduction of CO_2 to CO is a kinetically favourable option because it has a lower reaction barrier compared to one-electron and multi-electron reactions.[248,249] Bimetallic synergistic catalysts are commonly explored for CO synthesis with enhanced performance over their monometallic counterparts because of multielectron accumulation at the catalytic centers. The carboxylate exchange at the Hf_{12} cluster of **[Ru(bpy)$_2$(dbpydc)+Hf$_{12}$]-MOL** with metal complexes yielded bimetallic catalysts **M@[Ru(bpy)$_2$(dbpydc)+Hf$_{12}$]-MOL** (M = Mn or Re, X = Cl or Br), that possessed both Ru(N^N)$_3$ photosensitizer and M(CO)$_3$X catalyst for efficient photocatalytic CO_2 reduction (Fig. 30).[155] The molecular catalyst $[Ni(bpet)(H_2O)_2]^{2+}$ was encapsulated into a photo-responsive **[Ru(bpy)$_2$(bpydc)/bpdc+Zr$_6$]-MOF** to fabricate a composite **Ni⊂[Ru(bpy)$_2$(bpydc)/bpdc+Zr$_6$]-MOF** for the photocatalytic transformation of CO_2 to CO.[139] Artificial photocatalytic CO_2RR is a big challenge as the efficient

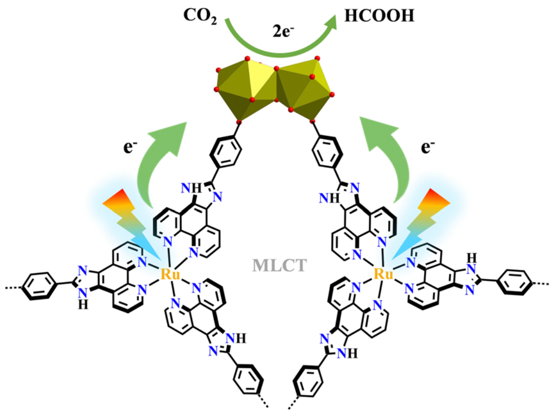

Fig. 29 Pathways of electron transfer from Ru(phenba)$_3$ to the catalytic Eu_2 oxo cluster in **[Ru(phenba)$_3$+Eu$_2$]-MOF**.[137]

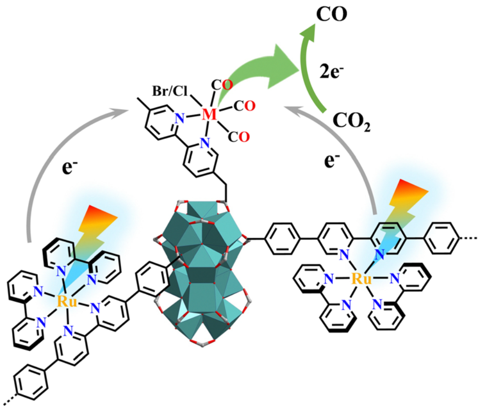

Fig. 30 Photocatalytic CO_2RR to CO occurred in **M@[Ru(bpy)$_2$(dbpydc)+Hf$_{12}$]-MOL**.[155]

cooperation of multiple functional units is difficult. Without use of an electron donor, the multifunctional photocatalyst **[Ru(ip)$_3$+Co]-MOF** could convert CO_2 to CO with a high CO production rate and nearly 100% selectivity accompanied by water oxidation to O_2. Suitable photocatalytic redox potentials, efficient electron-hole separation and CO_2 adsorption ability all contributed to this artificial photosynthesis.[59]

Syngas (a mixture of H_2 and CO) is a versatile fuel precursor for producing chemical and synthetic liquid fuels. Photocatalytic CO_2RR will open an avenue for consecutive production of syngas.[250] Zhang and collaborators reported a **Co@[Ru(bpy)$_2$(bpydc)/bpdc+Zr$_6$]-MOF** composite photocatalyst for efficient syngas production. Interestingly, the H_2/CO ratios could be well regulated by precisely adjusting the water content of the reaction solution and the molar ratio of PS/Cat in the network.[149]

Photoirradiation CO_2 hydrogenation to ethanol is of practical importance yet poses a significant challenge due to the formation of a C–C bond with an intact C–O bond. Lin and coworkers used low-intensity light to activate a **Cu@[Ru(bpy)$_2$(bpydc)/bpdc+Zr$_6$]-MOF** catalyst for the selective hydrogenation of CO_2 to C_2H_5OH. Under light illumination, $[Ru(N^\wedge N)_3]^*$ underwent single-electron-transfer to Cu^{2+} to generate Cu^+ which was active for C_2H_5OH production. In contrast, Cu^0 nanoparticles were formed as the active species for CH_3OH production under darkness (Fig. 31).[138]

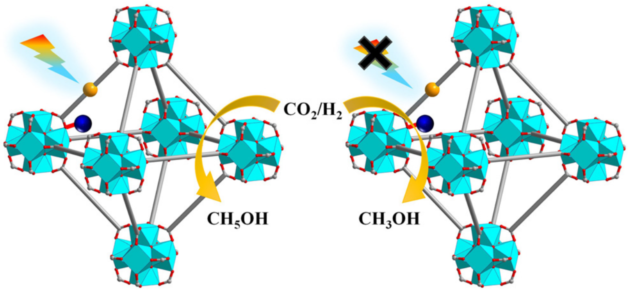

Fig. 31 Selective photocatalytic CO_2RR with or without light irradiation catalysed by **Cu@[Ru(bpy)$_2$(bpydc)/bpdc+Zr$_6$]-MOF**.[138]

7.3 Aerobic photooxidation

Aerobic photooxidation is very important in organic synthesis because photocatalysis provides a high-efficiency, safe and economic O_2 utilization for developing diverse aerobic organic transformations and O_2 could be transformed to other ROSs, such as H_2O_2, $^1O_2$, $^\bullet O_2^-$, and $^\bullet OH$.[251] ROSs of $^\bullet OH$, H_2O_2, $^\bullet O_2^-$ and $^1O_2$ could be generated in different ways. A stepwise reduction of O_2 respectively generates $^\bullet O^{2-}$, H_2O_2, and $^\bullet OH$.[251] The quantum yield of $^\bullet O_2^-$ is significantly higher, and its lifetime is only lower than H_2O_2. In the absence of reactants, $^\bullet O_2^-$ is converted to the stable H_2O_2 *via* a disproportionation process. The $^\bullet OH$ radical has the highest oxidation activity, thus its oxidation performance is almost limited by the substrate diffusion rate. In addition, $^\bullet OH$ is commonly pursued in photocatalytic organic decomposition. Although $^1O_2$ has a lifetime of ten milliseconds in air, it was shortened to only 3 μs in H_2O and thus it might be decayed by energy transfer with no chance of participating in any reaction.[251]

By combining three intrinsically nontoxic components, namely, photosensitizer, light, and tissue O_2 to generate cytotoxic ROS, photodynamic therapy provides an effective phototherapy against cancer.[252] Ultrathin MOLs facilitate the diffusion of ROS to cell milieu to exert cytotoxic effects.[50,156] Cationic **[Ir(ppy)$_2$(dbpydc)+Hf$_{12}$]-MOL** was built from Hf$_{12}$-SBUs and $[Ir(ppy)_2(H_2dbpydc)]^+$-metalloligand and then was loaded with POMs $\{P_2W_{18}\}$ to afford **$\{P_2W_{18}\}\subset$[Ir(ppy)$_2$(dbpydc)+Hf$_{12}$]-MOL**. Upon X-ray irradiation, **$\{P_2W_{18}\}\subset$[Ir(ppy)$_2$(dbpydc)+Hf$_{12}$]-MOL** significantly enhanced $^\bullet OH$ generation from Hf$_{12}$-SBUs, $^1O_2$ generation from $[Ir(ppy)_2(H_2dbpydc)]^+$-metalloligand, and $^\bullet O_2^-$ generation from $\{P_2W_{18}\}$, achieving synergistic cell killing by these ROSs (Fig. 32).[49]

Aerobic photocatalytic sulfide oxidation to sulphoxide is a green pathway for sulphoxide production using O_2 as an oxidant. Highly stable **[Ir(pqc)$_2$(phen)+Zr$_6$]-MOF** was constructed by $[Ir(pqc)_2(phen)]^+$-metalloigand linkers and Zr$_6$-SBUs. **[Ir(pqc)$_2$(phen)+Zr$_6$]-MOF** exhibited high catalytic activity upon aerobic photooxidation of sulfide into sulfoxide in water at room temperature.[48,142] Under visible light irradiation, the $[Ir(pqc)_2(phen)]^+$ photosensitizer was excited to a high-energy excited singlet state $^1\{[Ir(pqc)_2(phen)]^+\}^*$, which quickly underwent intersystem crossing to an excited triplet due to the highly efficient spin–orbit coupling. The $^3\{[Ir(pqc)_2(phen)]^+\}^*$ transferred an electron to O_2 to form $^\bullet O_2^-$ and generated $[Ir(pqc)_2(phen)]^{2+}$. Sulfide was oxidized by $[Ir(pqc)_2(phen)]^{2+}$ to generate a sulfide radical cation and achieve the regeneration of neutral $[Ir(pqc)_2(phen)]^+$ photosensitizer in the photocatalytic cycle. The sulfide radical cation reacted with the $^\bullet O_2^-$ to generate a persulfoxide intermediate, which further reacted with sulfide to afford the corresponding sulfoxides. In this system H_2O not only accelerated the conversion of persulfoxide into sulfoxide but also prevented the over oxidation of sulfoxide into sulfone.[48] Moreover, $^\bullet O_2^-$ was the main ROS for efficient photocatalytic sulfide oxidation. Interestingly, by changing the auxiliary ligand of the Ir(pqc)$_2$(N^N)-metalloligand, the excitation lifetime of the triplet state, the generation of ROS quantum

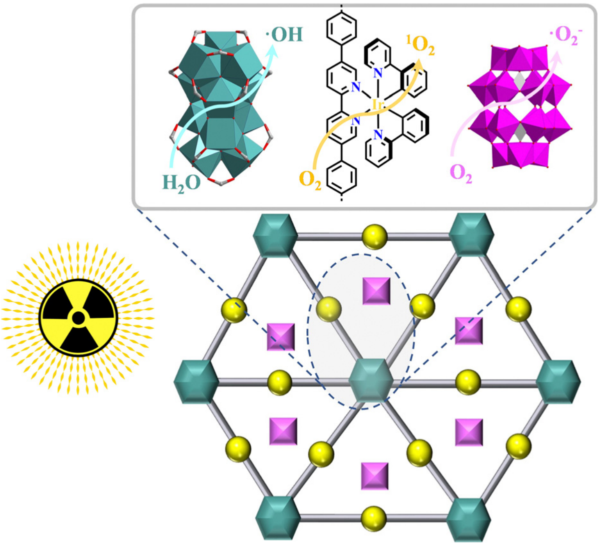

Fig. 32 Three distinct ROS generated from **{P_2W_{18}}⊂[Ir(ppy)$_2$(db-pydc)+Hf_{12}]-MOL** upon X-ray irradiation.[49]

yields, and the sulfide photooxidation efficiency could be tuned.[253] **Ru(bpy)$_2$(bpydc)@(bpydc+Ln$_6$)-MOFs** (Ln = Tb, Gd, Eu) showed excellent photocatalytic activity in sulfide oxidation with high conversion and sulfoxide selectivity under an O_2 atmosphere, $^{\bullet}O^{2-}$ was the main ROS and h^+ also took effect in oxidation. **Ru(bpy)$_2$(bpydc)@(bpydc+Ln$_6$)-MOFs** were excited by visible light and generated electrons and holes. Here, O_2 accepted an electron and produced $^{\bullet}O_2^-$, which further attacked sulfide, with the assistance of h^+, the active intermediate persulphoxide formed, and its reaction with another sulfide molecule led to the formation of sulfoxide products.[142] **[Ru(cptpy)$_2$+Ce]-MOF** was synthesized from $[Ru(cptpy)_2]^{2+}$-metalloligands and $Ce(NO_3)_3$. **[Ru(cptpy)$_2$+Ce]-MOF** exhibited high photocatalytic activities in sulfide oxidation, which is better than the isomorphic **[Ru(cptpy)$_2$+Zr]-MOF**, revealing the important role of Ln(III) ions in the photocatalytic process. The doping of Zr(IV) enhanced the chemical stability of **[Ru(cptpy)$_2$+Ce/Zr]-MOF**, and **[Ru(cptpy)$_2$+Ce/Zr]-MOF** possessed both high chemical stability and catalytic efficiency in photocatalytic sulfide oxidation.[254]

Overall photocatalytic water splitting is a great challenge. Thermodynamically, the conduction band/valence band position of the semiconductor must match the reduction/oxidation potential of water, so that the excited electron–hole pair has a sufficient ability to carry out overall water splitting. Dynamically, the slow desorption rate of H_2 and O_2 generated by photocatalytic water splitting on the surface of the material also becomes the kinetic limiting factor, and the desorption rate is slower than the recombination of photo-generated electrons and holes.[255–258] **HER-MOF** and **WOR-MOF** nanosheets were integrated into liposomal structures for separation of the photogenerated charges. For example, the **HER-MOF** were constructed from hydrophobically modified Hf_6 clusters and Zn–porphyrin or Pt–porphyrin linkers, while **WOR-MOF** were fabricated by Zr_{12} clusters and Ru(N^N)$_3$ or Ir(C^N)$_2$(N^N) metalloligands. The lipid membrane separated the oxidative and reductive components to prevent charges recombination, and this system was used in overall photocatalytic water splitting through the 'Z-scheme' electron-transfer.[259]

[Ru(bpy)$_2$(bpydc)/BTB+Zr$_6$]-MOF was assembled *via* the linkage of BTB-Zr$_6$ layers and $[Ru(bpy)_2(H_2bpydc)]^{2+}$-metalloligand, and it served as a highly efficient catalyst in the photooxidation reactions, including photooxidation of sulfide, coupling of amines and oxidative hydroxylation of arylboronic acids (Fig. 33). The main ROS of three types of reaction was $^{\bullet}O^{2-}$, and the generated ROS was determined by the photocatalyst itself.[260] Mesoporous **Ru(bpy)$_2$(bpydc)@(TPTB+Zr$_6$)-MOF** was composed of Zr$_6$ clusters and Ru(bpy)$_2$(H$_2$bpydc)-metalloligand, and it exhibited exceptional high photocatalytic activity in the oxidation of dihydroartemisinic acid to artemisinin.[118] The 3D diamondoid **(BPDCA+TAPM)-COF** had open (N^N)-sites, and the incorporation of the Ru(bpy)$_2$Cl$_2$ unit led to **Ru(N^N)$_3$@(BPDCA+TAPM)-COF**, which performed as a highly efficient, visible-light-mediated photocatalyst for the oxidative cyanation reaction of tertiary amines with excellent yields.[191]

7.4 Photocatalytic organic transformation

Organic transformations play a key role in the synthesis of pharmaceutical drugs and functional molecules. Photocatalytic reactions have appeared as a new tool to solve some critical problems met in the traditional reaction methods because photocatalysis could directly activate the substrates and bypass the reaction barrier. The last decade has witnessed the rapid development of photoredox catalysis.[6,219,261] In particular, Ru(N^N)$_3$ or Ir(C^N)$_2$(X^N) derivatives have been widely used as the photocatalyst.[262–264] A large number of Ru(N^N)$_3$ or Ir(C^N)$_2$(X^N) functionalized architectures have been explored for the photocatalytic organic transformation, including single-site catalysts,[116,118] dual active sites[115,135,136,141,265] and ternary active sites[158] for synergistic catalysis.

Ru(N^N)$_3$ or Ir(C^N)$_2$(X^N) derivatives acted as both photosensitizer and catalyst in the well-defined architectures. The **Ru(N^N)$_3$@(BPDCA+TAB)-COF** displayed unprecedented photocatalytic activity of visible light and achieved cross-

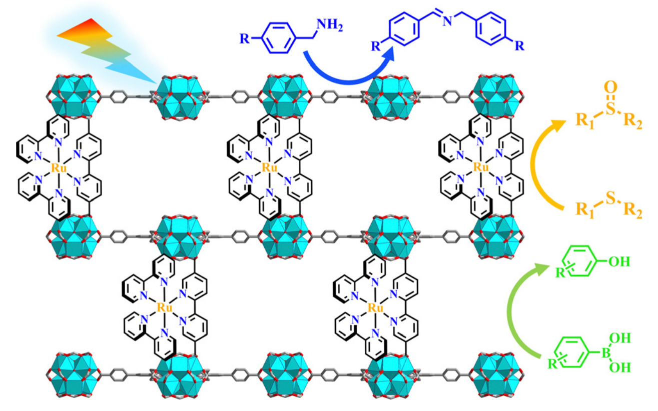

Fig. 33 Aerobic photooxidation catalysed by **[Ru(bpy)$_2$(bpydc)/BTB+Zr$_6$]-MOF**.[260]

dehydrogenation coupling of secondary amine and indole with an excellent rate (Scheme 1).[116] Mesoporous **Ru(bpy)$_2$(bpydc)@(TPTB+Zr$_6$)-MOF** photocatalyzed the aza-Henry reaction with high conversion yields (Scheme 2), showing a similar catalytic performance with [Ru(bpy)$_3$]$^{2+}$.[118] Stereoselectivity in photoredox reactions was very difficult to control. One strategy to achieve enantioselectivity in photoredox reactions is to combine a photoredox catalyst and a stereochemically controlled cocatalyst into one catalytic system.[266–268] **Δ/Λ-[Pd$_6$Ru$_8$]** metallasupramolecules had dual functionality of photoredox reactivity and stereoselectivity. The photoinduced regio- and enantioselective coupling of naphthols and its derivatives thereof was achieved in the confined chiral space of **[Pd$_6$Ru$_8$]**. The enantiomer cages encased naphthol guests, and then underwent a regionally specific 1,4-coupling, instead of the normal 1,1-coupling, forming 4-(2-hydroxy-1-naphthyl)-1,2-napthoquinones.[231] **Δ/Λ-[Pd$_6$Ru$_8$]** was also an effective supramolecular reactor to achieve the enantioselective cycloaddition of 1-subsituted acenaphthylene derivatives.[232]

In the well-defined architectures, Ru(N^N)$_3$ and Ir(C^N)$_2$(X^N) units are synergistic with another catalyst in the catalytic reactions. The proximity and cooperativity between different catalytic sites are key issues in the design of dual-functional catalytic systems.[269] The precise location of dual catalytic sites at porous architectures should be a feasible strategy.[115,135,136,141,265] The proximity of two catalytic components in the cavities of the frameworks greatly facilitates charge transfer from photosensitizing centers to catalytic centers, reaching a higher turnover number than the free counterpart.[135,136,265] Incorporation of Ni(N^N)Cl$_2$ Cat into **[Ir(dFCFppy)$_2$(dbpydc)/dbpydc+Zr$_{12}$]-MOL**,[265] **[Ir(dFCFppy)$_2$(dbpydc)+Hf$_{12}$]-MOL**,[135] **Ir(dFCFppy)$_2$(N^N)@(phendda+TAB)-COF** and **Ir(ppy)$_2$((N^N))@(Tp+abpy)-COF**[115,117] efficiently catalysed four important cross-coupling reactions with broad substrate scopes, including C–S cross-coupling between thiols and aryl iodides,[135,265] C–O cross-coupling between aryl bromides and alcohols,[135] and C–C cross-coupling between aryl bromides and potassium benzyltrifluoroborates (Scheme 3)[115,135] as well as C–N cross-coupling between iodides and amines.[117] For example, upon light irradiation, [Ir(dFCFppy)$_2$(H$_2$dbpydc)]$^+$ was excited to {[Ir(dFCFppy)$_2$(H$_2$dbpydc)]$^+$}* and it was quenched by thiol and NiCl$_2$ to generate the thiol radical and Ni$^+$–Cl. The binding of thiol and Ni$^+$–Cl formed Ni^{2+}–Cl–sulphide species (Fig. 34). The concomitantly obtained Ir(dFCFppy)$_2$(H$_2$dbpydc) returned to [Ir(dFCFppy)$_2$(H$_2$dbpydc)]$^+$ by transferring one electron to Ni^{2+}–Cl–sulphide thus formed Ni$^+$–sulphide. Oxidative addition of an aryl iodide to Ni$^+$–sulphide delivered a Ni^{3+}-complex, which underwent a facile reductive elimination process, leading to a C–S cross-coupled product and regeneration of Ni^{2+}–Cl. The distance between the Ir(III) photosensitizer and Ni(II) catalytic center was shortened to only 0.6 nm, which facilitated both electron and thiophenol radical transfers and significantly enhanced its photocatalytic activity.[265] Multifunctional **OTf@[Ir(dFCFppy)$_2$(dbpydc)+Hf$_{12}$]-MOL** had a synergistic catalytic performance in dehydrogenative cross-couplings of heteroarenes with unactivated alkanes, amines, and ethers. Furthermore, it could also catalyse late-stage functionalization of bioactive and drug molecules such as caffeine, Fasudil, and Metyrapone.[136] A mesoporous **[OTf/Ir(ppy)$_2$(bpydc)]@(bpydc+Al)-MOF** had both strong Lewis acidic Al-OTf sites and photoredox sites, which effectively catalysed reductive cross-coupling to afford new azaarene derivatives.[141] The employment of a homogeneous Au-catalyst typically required high catalyst loadings due to the relatively low reactivity of Au complexes and rapid catalyst deactivation. Deactivation of Au catalysts *via* a ligand redistribution formed [Au(phosphine)]$^+$ and unstable Au$^+$ complexes, then Au$^+$ complexes disproportionated into catalytically inactive Au^{3+} species and Au^0 nanoparticles.[270] MOLs could hierarchically integrate photosensitizers and Au catalysts together, not only preventing Au catalyst deactivation but also enhancing photoredox catalytic activities with proximately placed photosensitizers and {Au[4-(diphenylphosphino)phenylacetate]}Cl. **[Au/Ru(N^N)$_3$]@(BPY+Hf$_6$)-MOL** was built from Ru(bpy)$_2$Cl$_2$, [Au(phosphine)]Cl, H$_3$BPY ligands and Hf$_6$ SBUs. Ru(bpy)$_2$(N^N) photosensitizer and Au$^+$ catalysts worked synergistically for the cross-coupling of allenoates, alkenes, or alkynes.[271]

The design of functional architectures with three or more catalytic centers remains a challenge.[272] A multifunctional catalyst allows the combination of multiple transformations in a one-pot synthetic route, rather than the traditional stop-and-go approach.[273] With three synergistic active sites, **OTf/Co@[Ru(bpy)$_2$(dbpydc)+Hf$_{12}$]-MOL** contained a Ru(bpy)$_2$(N^N) photosensitizer, strong Lewis acid OTf-Hf$_{12}$-SBUs and hydrogen transfer catalyst [Co(dimethylglyoxime)$_2$(4-pyridinepropionate)]Cl, which efficiently catalysed dehydrogenative tandem transformations (Scheme 4). The hierarchical integration of three different catalytic centers into the MOL could prevent mutual inactivation

Scheme 1 Photocatalytic cross-dehydrogenative coupling of secondary amines with indoles catalysed by **Ru(N^N)$_3$@(BPDCA+TAB)-COF**.[116]

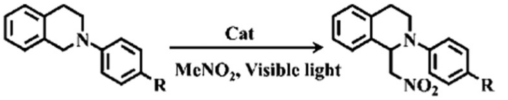

Scheme 2 Aza-Henry reactions photocatalyzed by **Ru(bpy)$_2$(bpydc)@(TPTB+Zr$_6$)-MOF**.[118]

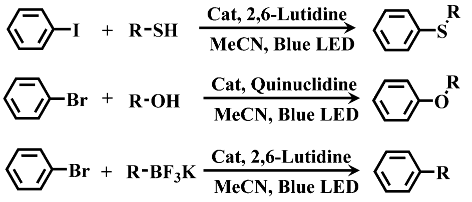

Scheme 3 C–S, C–O, and C–C cross-coupling reactions photocatalyzed by **Ni@[Ir(dFCFppy)$_2$(dbpydc)+Hf$_{12}$]-MOL**.[135]

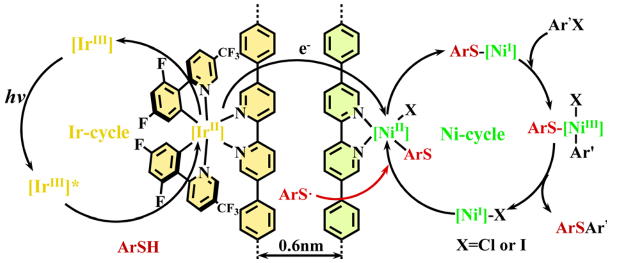

Fig. 34 Proposed mechanism for the C–S cross-coupling reaction catalysed by **Ni@[Ir(dFCFppy)$_2$(dbpydc)/dbpydc+Zr$_{12}$]-MOL**.[265]

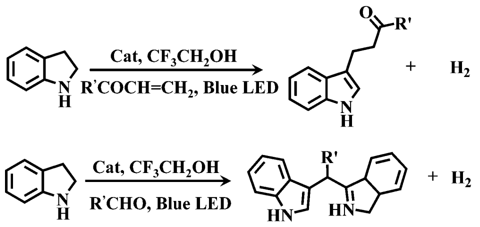

Scheme 4 Dehydrogenative tandem transformations of indolines photocatalyzed by **OTf/Co@[Ru(bpy)$_2$(dbpydc)+Hf$_{12}$]-MOL**.[158]

and promote charge transfer to enhance the synergistic tandem catalytic activity. Under light irradiation, the excited {[Ru(bpy)$_2$(N^N)]$^{2+}$}* transferred one electron to the Co^{3+} unit and generated a Co^{2+} unit and [Ru(bpy)$_2$(N^N)]$^{3+}$, then indoline was oxidated to the radical cation intermediate by [Ru(bpy)$_2$(N^N)]$^{3+}$. Deprotonation of the radical cation intermediate formed the α-carbon radical, and its radical addition reaction with Co^{2+} formed Co^{3+}–C bonded intermediate. Subsequently, the β-H elimination from the Co^{3+}–C intermediate produced the indole and Co^{3+}–H intermediate, and Co^{3+}–H was protonated and enabled the H$_2$ production and regeneration of Co^{3+} catalysts. Simultaneously, upon coordinating to the strongly Lewis acidic Hf$_{12}$ SBUs, vinyl ketone became electron deficient and attacked the electron rich β-position of indole, and the resulting intermediate further reacted with vinyl ketone to form the corresponding product.[158]

8. Summary and future prospects

Here we reviewed the application of Ru(N^N)$_3$ and Ir(C^N)$_2$(X^N) based architectures for in-light-driven catalysis, which provide an interesting platform for photosynthesis by organizing photoactive components in well-organised architectures. The incorporation of Ru(N^N)$_3$ and Ir(C^N)$_2$(X^N) building blocks into well-defined skeletons can create interesting architectures with novel structures and the required photofunction, because the structural aesthetics and functional advantages of Ru(N^N)$_3$ or Ir(C^N)$_2$(X^N) are readily inherited in the target architectures, and the combination of functional tectons, nano-cavity, crystalline network and Lewis acid site produced new photofunctional entities. The absorption ability of light, absorption band, and the diversity of structures could be enhanced and broadened by the integration of Ru(N^N)$_3$ or Ir(C^N)$_2$(X^N) into distinct architectures. These Ru(N^N)$_3$ and Ir(C^N)$_2$(X^N) functionalized architectures exhibited novel photocatalytic performances with a synergistic catalytic effect, high catalytic activity, product selectivity and recyclability. As highlighted in POMs⊂Ru(Ir)-MOF, the components of the photosensitizer and POMs were organised in close proximity, to promote the photogenerated electron transfer from the photosensitizer to POMs, and the accumulation of electrons at POMs achieved photocatalytic hydrogen production. The integration of Ir(C^N)$_2$(N^N) and Ni^{2+} into the porous network of 2D (N^N)-COF enabled highly efficient photocatalysis of C–C or C–N cross-couplings. In the **[Pd$_6$Ru$_8$]** cage, the supramolecular interactions between host and guest can regulate the redox potentials of the photosensitizer and catalyst, enhance charger transfer, and stabilize the catalytic intermediates, resulting in special photocatalytic activity.

The design and synthesis of Ru(N^N)$_3$ and Ir(C^N)$_2$(X^N) based architectures is ongoing research, while the use of these novel complexes for photosynthesis still remains underexplored. There are still some serious problems needed to be solved compared with plant photosynthesis. (1) Understanding of photo-generated charge and energy transfer processes, efficient charge separation, and stabilization of unstable intermediates should provide more insights into the fundamental mechanistic aspects for the development of efficient photocatalysts. (2) The simultaneous consumption of both electrons and holes is difficult, and the addition of sacrificial agents results in resource waste and pollution. (3) Ru(N^N)$_3$ and Ir(C^N)$_2$(X^N) functionalized architectures still face limited broadband light absorption and low Φ_{PL} due to inefficient separation of photogenerated electrons and holes. (4) The design and construction of Ru(N^N)$_3$ and Ir(C^N)$_2$(X^N) photo-functionalized architectures remain sustainable developments because the architecture type, architecture porosity, linkage type and alignment mode of the photosensitizer and catalyst, and the introduction of a guest have a great influence on the functionality. These architectures showing interesting catalytic properties are also expected to show other photophysical properties like multi-photon absorption cross-sections, and second and third harmonic generations. Furthermore, the architectures may be able to include both the Ru(N^N)$_3$ and Ir(C^N)$_2$(X^N) moieties into the same architectures. Although this has not been accomplished successfully, the synergistic effect of the presence of these photofunctional metal complexes in the same materials will be of immense academic interest and may shed more light on understanding the design principles of new functional materials. The incorporation of Ru(N^N)$_3$ and Ir(C^N)$_2$(X^N) moieties into other well-defined architectures like a molecular sieve could produce stable mesoporous photocatalysts. Immobilizing these Ru(N^N)$_3$ or Ir(C^N)$_2$(X^N) based complexes on a conductive supporter will allow their implementation on photoelectrochemical devices. These are expected to promote their closer commercial applications.

Abbreviations

MLCT	Metal-to-ligand charge transfer
ILCT	Intraligand charge transfer
MOFs	Metal–organic frameworks
COFs	Covalent organic frameworks
SOFs	Supramolecular organic framework
MOL	Metal–organic layer
2D	Two-dimensional
3D	Three-dimensional
Φ_{PL}	Emission quantum yields
bpy	2,2′-Bipyridine
H-ppy	2-Phenylpyridine
SBUs	Secondary building units
PSM	Post-synthetic modification
H_2bpydc	2,2′-Bipyridine-5,5′-dicarboxylic acid
H_4TPTB	5′,5‴-Bis(4-carboxylatophenyl)-4‴,6′-dimethoxy-[1,1′:3′,1″:4″,1‴:3⁗,1⁗-quinquephenyl]-4,4⁗-dicarboxylate
H_2bpdc	4,4′-Biphenyldicarboxylic acid
H-pqc	H-2-Phenylquinoline-4-carboxylic acid
H_3BPY	4′,6′-Dibenzoato-[2,2′-bipyridine]-4-carboxylic acid
Hip	1*H*-Imidazo[4,5-*f*][1,10]phenanthroline
H-H_2dcppy	2-(3-Carboxyphenyl)pyridine-4-carboxylic acid
H_2dcbpy	2,2′-Bipyridine-4,4′-dicarboxylic acid
H_2dbpydc	4,4′-([2,2′-Bipyridine]-5,5′-diyl)dibenzoic acid
H_4dpbpy	2,2′-Bipyridine-4,4′-bis(phosphonic acid)
phenba	4-(1*H*-Imidazo[4,5-*f*][1,10]phenanthrolin-2-yl)benzoic acid
phen	1,10-Phenanthroline
H-ppy-COOH	3-(Pyridin-2-yl)benzoic acid
cptpy	4′-(4-Carboxyphenyl)-terpyridine
Ln	Lanthanides
H_3BTB	1,3,5-Benzenetribenzoate
HMBA	2-[5′-Methyl-(2,2′-bipyridin)-5-yl]acetate
bpy-OEt	5,5′-Bis(diethoxymethyl)-2,2′-bipyridine
ETTA	4,4′,4″,4‴-(Ethene-1,1,2,2-tetrayl)tetraaniline
TPB	1,2,4,5-Tetrakis-(4-aminolphenyl)benzene
BPDCA	2,2′-Bipyridine-5,5′-dicarbaldehyde
TAB	1,3,5-Tris-(4-aminophenyl) benzene
ETTBA	4′,4‴,4′′′′′,4′′′′′′′-(Ethene-1,1,2,2-tetrayl)tetrakis([1,1′-biphenyl]-4-amine)
phendda	4,4′-(1,10-Phenanthroline-3,8-diyl)dibenzaldehyde
abpy	5,5′-Diamino-2,2′-bipyridine
Tp	1,3,5-Triformylphloroglucinol
TAPM	Tetra(*p*-aminophenyl)methane
TPMB	Tetrakisphenylmethane borate
MeCN	Acetonitrile
TEPM	Tetra(4-ethynylphenyl)methane
piphen	2-(Pyridin-3-yl)-1*H*-imidazo[4,5-*f*][1,10]phenanthroline
TTF	Tetrathiafulvalene
BINOL	1,1′-Bis(2-naphthol)
H-dFCFppy	2-(2,4-Difluorophenyl)-5-(trifluoromethyl)pyridine
H-ppy-CHO	4-(2-Pyridyl)benzaldehyde
tbubpy	4,4′-Di(*tert*-butyl)-2,2′-bipyridine
H-mesppy	2-Phenyl-4-mesitylpyridinato
qpy	4,4′:2′,2″,4″,4‴-Quaterpyridine
H-dFmesppy	2-(4,6-Difluorophenyl)-4-mesitylpyridinato
H-dFppy	(2-(2,4-Difluorophenyl)-4-phenyl)pyridine
H-appy	4-(2-Pyridinyl)phenylamine
tpmc	Tris(4-pyridyl-methyl)-cyclotriguaiacylene
ttpadtc	2,7,12-Trimethoxy-3,8,13-tris(4,4′-pyridylazophenylcarboxy)-10,15-dihydro-5*H*-tribenzo[*a*,*d*,*g*] cyclononene
bpet	1,2-Bis[(pyridin-2-ylmethyl)thio]ethane
OTf	Triflate
TPT	2,4,6-Tri(pyridin-4-yl)-1,3,5-triazine
HOMO	Highest occupied molecular orbital
LUMO	Lowest unoccupied molecular orbital
PS	Photosensitizer
Cat	Catalyst
D	Electron donor
A	Electron acceptor
POMs	Polyoxometalates
$\{P_2W_{18}\}$	$[P_2W1_8O_{62}]^{6-}$
$\{PW_{12}\}$	$[PW_{12}O_{40}]^{3-}$
$\{Ni_4P_2\}$	$[Ni_4(H_2O)_2(PW_9O_{34})_2]^{10-}$
CO_2RR	Carbon dioxide reduction reactions
CO_2	Carbon dioxide
HCOOH	Formate
CO	Carbon monoxide
HCHO	Formaldehyde
CH_3OH	Methanol
CH_4	Methane
O_2	Oxygen
ROS	Reactive oxygen species
H_2O_2	Hydrogen peroxide
$^1O_2$	Singlet oxygen
$^\bullet O_2^-$	Superoxide radical
$^\bullet OH$	Hydroxyl radical
HER	Hydrogen evolution reaction.

Conflicts of interest

There are no conflicts to declare.

Acknowledgements

This work was supported by the National Science Foundation of China (21971011 and 21831001).

References

1 S. Pete, N. Roy, B. Kar and P. Paira, *Coord. Chem. Rev.*, 2022, **460**, 214462–214516.

2 A. Wragg, M. R. Gill, D. Turton, H. Adams, T. M. Roseveare, C. Smythe, X. Su and J. A. Thomas, *Chem. – Eur. J.*, 2014, **20**, 14004–14011.

3 A. J. Atkins and L. Gonzalez, *J. Phys. Chem. Lett.*, 2017, **8**, 3840–3845.

4 Y. Cho, S. Kim, M. Cho, K. Wee, H. Son, W. Han, D. W. Cho and S. O. Kang, *Phys. Chem. Chem. Phys.*, 2016, **18**, 15162–15169.

5 S. Verma, P. Kar, A. Das and H. N. Ghosh, *Dalton Trans.*, 2011, **40**, 9765–9773.

6 C. K. Prier, D. A. Rankic and D. W. C. MacMillan, *Chem. Rev.*, 2013, **113**, 5322–5363.

7 A. F. Henwood and E. Zysman-Colman, *Top. Curr. Chem.*, 2016, **374**, 36–76.

8 L. Flamigni, A. Barbieri, C. Sabatini, B. Ventura and F. Barigelletti, *Top. Curr. Chem.*, 2007, **281**, 143–203.

9 Z. Chang, D. Yang, J. Xu, T. Hu and X. Bu, *Adv. Mater.*, 2015, **27**, 5432–5441.

10 W. Cui, G. Zhang, T. Hu and X. Bu, *Coord. Chem. Rev.*, 2019, **387**, 79–120.

11 X. Ge, R. Wong, A. Anisa and S. Ma, *Biomaterials*, 2022, **281**, 121322–121339.

12 B. Gibbons, M. Cai and A. J. Morris, *J. Am. Chem. Soc.*, 2022, **144**, 17723–17736.

13 Y. Song, Q. Sun, B. Aguila and S. Ma, *Adv. Sci.*, 2019, **6**, 1801410–1801443.

14 H. Vardhan, A. Nafady, A. M. Al-Enizi and S. Ma, *Nanoscale*, 2019, **11**, 21679–21708.

15 Z. Chen, J. Wang, M. Hao, Y. Xie, X. Liu, H. Yang, G. I. N. Waterhouse, X. Wang and S. Ma, *Nat. Commun.*, 2023, **14**, 1106.

16 S. Chakraborty and G. R. Newkome, *Chem. Soc. Rev.*, 2018, **47**, 3991–4016.

17 M. M. J. Smulders, I. A. Riddell, C. Browne and J. R. Nitschke, *Chem. Soc. Rev.*, 2013, **42**, 1728–1754.

18 R. W. Hogue, S. Singh and S. Brooker, *Chem. Soc. Rev.*, 2018, **47**, 7303–7338.

19 D. Chakraborty and P. S. Mukherjee, *Chem. Commun.*, 2022, **58**, 5558–5573.

20 W. Liu, A. G. Oliver and B. D. Smith, *J. Am. Chem. Soc.*, 2018, **140**, 6810–6813.

21 P. K. Mandal, B. Kauffmann, H. Destecroix, Y. Ferrand, A. P. Davis and I. Huc, *Chem. Commun.*, 2016, **52**, 9355–9358.

22 Y. Huang, R. Gao, M. Liu, L. Chen, X. Ni, X. Xiao, H. Cong, Q. Zhu, K. Chen and Z. Tao, *Angew. Chem., Int. Ed.*, 2021, **60**, 15166–15191.

23 M. Shen, X. Lin, J. Luo, W. Li, Y. Ye and X. Wang, *Mol. Syst. Des. Eng.*, 2022, **7**, 1570–1587.

24 Y. Zhou, G. Zhang, B. Li and L. Wu, *ACS Appl. Mater. Interfaces*, 2020, **12**, 30761–30769.

25 L. Yue, S. Wang, D. Zhou, H. Zhang, B. Li and L. Wu, *Nat. Commun.*, 2016, **7**, 10742–10751.

26 J. M. Lee and A. I. Cooper, *Chem. Rev.*, 2020, **120**, 2171–2214.

27 K. Yang, Y. Ban and W. Yang, *J. Membr. Sci.*, 2021, **639**, 119771–119777.

28 A. H. Assen, T. Virdis, W. De Moor, A. Moussa, M. Eddaoudi, G. Baron, J. F. M. Denayer and Y. Belmabkhout, *Chem. Eng. J.*, 2021, **413**, 127388–127395.

29 S. Zhang, Y. Zheng, H. An, B. Aguila, C. Yang, Y. Dong, W. Xie, P. Cheng, Z. Zhang, Y. Chen and S. Ma, *Angew. Chem., Int. Ed.*, 2018, **57**, 16754–16759.

30 H. Chen, C. Jin, X. Chen, J. Yu, D. Yan, P. Cheng, Z. Zhang, L. Zhao and Y. Chen, *Chem. Eng. J.*, 2022, **444**, 136624–136631.

31 M. Yoshizawa, J. K. Klosterman and M. Fujita, *Angew. Chem., Int. Ed.*, 2009, **48**, 3418–3438.

32 X. Li, J. Wu, L. Wang, C. He, L. Chen, Y. Jiao and C. Duan, *Angew. Chem., Int. Ed.*, 2020, **59**, 6420–6427.

33 G. Zhang, B. Li, Y. Zhou, X. Chen, B. Li, Z. Lu and L. Wu, *Nat. Commun.*, 2020, **11**, 425–433.

34 H. J. Zhou and S. Kitagawa, *Chem. Soc. Rev.*, 2014, **43**, 5415–5418.

35 S. Huang, N. Liu, Y. Ling and H. Luo, *Chem. – Asian J.*, 2017, **12**, 3110–3113.

36 X. Li, J. Wu, C. He, R. Zhang and C. Duan, *Chem. Commun.*, 2016, **52**, 5104–5107.

37 Y. Song, Y. Pi, X. Feng, K. Ni, Z. Xu, J. S. Chen, Z. Li and W. Lin, *J. Am. Chem. Soc.*, 2020, **142**, 6866–6871.

38 J. Lin, X. Hu, P. Zhang, A. Van Rynbach, D. N. Beratan, C. A. Kent, B. P. Mehl, J. M. Papanikolas, T. J. Meyer, W. Lin, S. S. Skourtis and M. Constantinou, *J. Phys. Chem. C*, 2013, **117**, 22250–22259.

39 A. Schmidt, M. Hollering, J. Han, A. Casini and F. E. Kuehn, *Dalton Trans.*, 2016, **45**, 12297–12300.

40 J. D. Knoll, S. M. Arachchige and K. J. Brewer, *ChemSusChem*, 2011, **4**, 252–261.

41 C. Hou, T. Li, S. Cao, Y. Chen and W. Fu, *J. Mater. Chem. A*, 2015, **3**, 10386–10394.

42 L. Zhang, S. Yin, M. Pan, W. Liao, J. Zhang, H. Wang and C. Su, *J. Mater. Chem. A*, 2017, **5**, 9807–9814.

43 C. Wang, Z. Xie, K. E. DeKrafft and W. Lin, *J. Am. Chem. Soc.*, 2011, **133**, 13445–13454.

44 G. Lan, K. Ni, E. You, M. Wang, A. Culbert, X. Jiang and W. Lin, *J. Am. Chem. Soc.*, 2019, **141**, 18964–18969.

45 H. Iranmanesh, K. S. A. Arachchige, M. Bhadbhade, W. A. Donald, J. Y. Liew, K. T. C. Liu, E. T. Luis, E. G. Moore, J. R. Price, H. Yan, J. Yang and J. E. Beves, *Inorg. Chem.*, 2016, **55**, 12737–12751.

46 E. T. Luis, H. Iranmanesh, K. S. A. Arachchige, W. A. Donald, G. Quach, E. G. Moore and J. E. Beves, *Inorg. Chem.*, 2018, **57**, 8476–8486.

47 D. Kim, D. R. Whang and S. Y. Park, *J. Am. Chem. Soc.*, 2016, **138**, 8698–8701.

48 L. Wei and B. Ye, *ACS Appl. Mater. Interfaces*, 2019, **11**, 41448–41457.

49 G. Lan, K. Ni, S. S. Veroneau, T. Luo, E. You and W. Lin, *J. Am. Chem. Soc.*, 2019, **141**, 6859–6863.

50 G. Lan, K. Ni, S. S. Veroneau, Y. Song and W. Lin, *J. Am. Chem. Soc.*, 2018, **140**, 16971–16975.

51 C. Xu, A. Guenet, N. Kyritsakas, J. Planeix and M. W. Hosseini, *Inorg. Chem.*, 2015, **54**, 10429–10439.

52 Z. Xu, Y. Luo, D. Zhang, H. Wang, X. Sun and Z. Li, *Green Chem.*, 2020, **22**, 136–143.

53 C. E. Hauke, A. N. Oldacre, C. R. P. Fulong, A. E. Friedman and T. R. Cook, *Inorg. Chem.*, 2017, **57**, 3587–3595.

54 L. Wang, Z. Xie, S. Dang and Z. Sun, *Chem. – Eur. J.*, 2017, **23**, 2852–2857.

55 H. Ahmad, D. Ghosh and J. A. Thomas, *Chem. Commun.*, 2014, **50**, 3859–3861.

56 V. E. Pritchard, D. R. Martir, S. Oldknow, S. Kai, S. Hiraoka, N. J. Cookson, E. Zysman-Colman and M. J. Hardie, *Chem. – Eur. J.*, 2017, **23**, 6290–6294.

57 L. Li, S. Zhang, L. Xu, L. Han, Z. Chen and J. Luo, *Inorg. Chem.*, 2013, **52**, 12323–12325.

58 C. Li, Y. Wang, Y. Lu, J. Guo, C. Zhu, H. He, X. Duan, M. Pan and C. Su, *Chin. Chem. Lett.*, 2020, **31**, 1183–1187.

59 N. Huang, J. Shen, X. Zhang, P. Liao, J. Zhang and X. Chen, *J. Am. Chem. Soc.*, 2022, **144**, 8676–8682.

60 K. Wu, K. Li, Y. Hou, M. Pan, L. Zhang, L. Chen and C. Su, *Nat. Commun.*, 2016, **7**, 10487–10496.

61 L. Martins, L. K. Macreadie, D. Sensharma, S. Vaesen, X. Zhang, J. J. Gough, M. O'Doherty, N. Zhu, M. Ruether, J. E. O'Brien, A. L. Bradley and W. Schmitt, *Chem. Commun.*, 2019, **55**, 5013–5016.

62 C. Liao, K. Fan, S. Bao, H. Fan, X. Wang, Z. Hu, M. Kurmoo and L. Zheng, *Chem. Commun.*, 2019, **55**, 13920–13923.

63 Z. Xie, L. Ma, K. E. DeKrafft, A. Jin and W. Lin, *J. Am. Chem. Soc.*, 2010, **132**, 922–923.

64 J. Wu, X. Li, P. Wu, Z. Shi, L. Chen, R. Zhang, C. He and C. Duan, *Chem. Mater.*, 2022, **34**, 4471–4478.

65 X. Li, J. Wu, L. Chen, X. Zhong, C. He, R. Zhang and C. Duan, *Chem. Commun.*, 2016, **52**, 9628–9631.

66 C. A. Kent, B. P. Mehl, L. Ma, J. M. Papanikolas, T. J. Meyer and W. Lin, *J. Am. Chem. Soc.*, 2010, **132**, 12767–12769.

67 D. P. August, J. Jaramillo-Garcia, D. A. Leigh, A. Valero and I. J. Vitorica-Yrezabal, *J. Am. Chem. Soc.*, 2021, **143**, 1154–1161.

68 A. Kobayashi, T. Ohba, E. Saitoh, Y. Suzuki, S. Noro, H. Chang and M. Kato, *Inorg. Chem.*, 2014, **53**, 2910–2921.

69 X. Li, S. Yu, B. Yang, J. Tian, H. Wang, D. Zhang, Y. Liu and Z. Li, *Sci. China: Chem.*, 2018, **61**, 830–835.

70 J. Tian, Z. Xu, D. Zhang, H. Wang, S. Xie, D. Xu, Y. Ren, H. Wang, Y. Liu and Z. Li, *Nat. Commun.*, 2016, **7**, 11580–11588.

71 W. Han, Y. Liu, X. Yan, Y. Jiang, J. Zhang and Z. Gu, *Angew. Chem., Int. Ed.*, 2022, **61**, e202208791.

72 H. Yin, J. Yang and X. Yin, *Anal. Chem.*, 2017, **89**, 13434–13440.

73 J. S. Z. Qiao, J. Zhang, J. Yu, M. Jaroniec and S. Z. Qiao, *Chem. Soc. Rev.*, 2014, **43**, 7787–7812.

74 H. Lv, W. Guo, K. Wu, Z. Chen, J. Bacsa, D. G. Musaev, Y. V. Geletii, S. M. Lauinger, T. Lian and C. L. Hill, *J. Am. Chem. Soc.*, 2014, **136**, 14015–14018.

75 X. Han, C. Qin, X. Wang, Y. Tan, X. Zhao and E. Wang, *Appl. Catal., B*, 2017, **211**, 349–356.

76 X. Zhao, J. Zhou, C. Sun, S. You, X. Wang and Z. Su, *Nanotechnology*, 2020, **31**, 255402–255407.

77 H. Xu, S. You, Z. Lang, Y. Sun, C. Sun, J. Zhou, X. Wang, Z. Kang and Z. Su, *Chem. – Eur. J.*, 2020, **26**, 2735–2740.

78 L. Qiao, M. Song, A. Geng and S. Yao, *Chin. Chem. Lett.*, 2019, **30**, 1273–1276.

79 J. Liu, S. Huang and G. Yang, *Sci. Sin.: Chim.*, 2020, **50**, 986–1000.

80 I. Bazzan, A. Volpe, A. Dolbecq, M. Natali, A. Sartorel, P. Mialane and M. Bonchio, *Catal. Today*, 2017, **290**, 39–50.

81 A. Lemos, C. Lemaire and A. Luxen, *Adv. Synth. Catal.*, 2019, **361**, 1500–1537.

82 C. S. Yeung, *Angew. Chem., Int. Ed.*, 2019, **58**, 5491–5502.

83 Q. Zhou, Y. Zou, L. Lu and W. Xiao, *Angew. Chem., Int. Ed.*, 2019, **58**, 1586–1604.

84 Y. You and W. Nam, *Chem. Soc. Rev.*, 2012, **41**, 761–784.

85 M. A. Baldo, M. E. Thompson and S. R. Forrest, *Nature*, 2000, **403**, 750–753.

86 W. Zhang, F. Zhang, Y. Wang, B. Song, R. Zhang and J. Yuan, *Inorg. Chem.*, 2017, **56**, 1309–1318.

87 G. B. Damas, D. A. Ivashchenko, I. Rivalta and C. M. Araujo, *Sustainable Energy Fuels*, 2021, **5**, 6066–6076.

88 I. N. Mills, J. A. Porras and S. Bernhard, *Acc. Chem. Res.*, 2018, **51**, 352–364.

89 K. K. Lo, K. Y. Zhang, S. Leung and M. Tang, *Angew. Chem., Int. Ed.*, 2008, **47**, 2213–2216.

90 H. Wu, T. Yang, Q. Zhao, J. Zhou, C. Li and F. Li, *Dalton Trans.*, 2011, **40**, 1969–1976.

91 M. Veerapandian, P. K. Avti and V. Ravichandiran, *Colloids Surf., B*, 2017, **154**, 315–320.

92 S. K. Pagire, N. Kumagai and M. Shibasaki, *Org. Lett.*, 2020, **22**, 7853–7858.

93 V. Reddy Yatham, Y. Shen and R. Martin, *Angew. Chem., Int. Ed.*, 2017, **56**, 10915–10919.

94 H. A. Sakai and D. W. C. MacMillan, *J. Am. Chem. Soc.*, 2022, **144**, 6185–6192.

95 Y. Liang, X. Zhang and D. W. C. MacMillan, *Nature*, 2018, **559**, 83–93.

96 J. C. K. Chu and T. Rovis, *Nature*, 2016, **539**, 272–275.

97 J. D. Cuthbertson and D. W. C. MacMillan, *Nature*, 2015, **519**, 74–77.

98 Y. Y. Loh, K. Nagao, A. J. Hoover, D. Hesk, N. R. Rivera, S. L. Colletti, I. W. Davies and D. W. C. MacMillan, *Science*, 2017, **358**, 1182.

99 K. Fan, S. Bao, R. Huo, X. Huang, Y. Liu, Z. Yu, M. Kurmoo and L. Zheng, *Inorg. Chem. Front.*, 2020, **7**, 4580–4592.

100 Z. He, C. Kim, L. Lin, T. H. Jeon, S. Lin, X. Wang and W. Choi, *Nano Energy*, 2017, **42**, 58–68.

101 Q. Lin, X. Bu, C. Mao, X. Zhao, K. Sasan and P. Feng, *J. Am. Chem. Soc.*, 2015, **137**, 6184–6187.

102 W. Zhou, W. Li, J. Wang, Y. Qu, Y. Yang, Y. Xie, K. Zhang, L. Wang, H. Fu and D. Zhao, *J. Am. Chem. Soc.*, 2014, **136**, 9280–9283.

103 J. Xiao, D. Li and H. Jiang, *Sci. Sin.: Chim.*, 2018, **48**, 1058–1075.

104 S. Yu, Q. Qi, B. Yang, H. Wang, D. Zhang, Y. Liu and Z. Li, *Small*, 2018, **14**, 1801037–1801043.

105 Z. Gao, Z. Wang, L. Wei, G. Yin, J. Tian, C. Liu, H. Wang, D. Zhang, Y. Zhang, X. Li, Y. Liu and Z. Li, *ACS Appl. Mater. Interfaces*, 2019, **12**, 1404–1411.

106 X. Yu and S. M. Cohen, *J. Am. Chem. Soc.*, 2016, **138**, 12320–12323.

107 C. Lim, M. D. Ryan, B. G. McCarthy, J. C. Theriot, S. M. Sartor, N. H. Damrauer, C. B. Musgrave and G. M. Miyake, *J. Am. Chem. Soc.*, 2017, **139**, 348–355.

108 S. You, J. Zhou, M. Chen, C. Sun, X. Qi, A. Yousaf, X. Wang and Z. Su, *J. Catal.*, 2020, **392**, 49–55.

109 H. Wang, L. Zhang, Z. Chen, J. Hu, S. Li, Z. Wang, J. Liu and X. Wang, *Chem. Soc. Rev.*, 2014, **43**, 5234–5244.

110 S. Bai, J. Ge, L. Wang, M. Gong, M. Deng, Q. Kong, L. Song, J. Jiang, Q. Zhang, Y. Luo, Y. Xie and Y. Xiong, *Adv. Mater.*, 2014, **26**, 5689.

111 A. Kudo and Y. Miseki, *Chem. Soc. Rev.*, 2009, **38**, 253–278.

112 X. Fang, Q. Shang, Y. Wang, L. Jiao, T. Yao, Y. Li, Q. Zhang, Y. Luo and H. Jiang, *Adv. Mater.*, 2018, **30**, 1075112–1075118.

113 J. Dong, X. Han, Y. Liu, H. Li and Y. Cui, *Angew. Chem., Int. Ed.*, 2020, **59**, 13722–13733.

114 Z. Zhang, T. Zhang, C. Wang, Z. Lin, L. Long and W. Lin, *J. Am. Chem. Soc.*, 2015, **137**, 3197–3200.

115 A. López-Magano, B. Ortín-Rubio, I. Imaz, D. Maspoch, J. Alemán and R. Mas-Ballesté, *ACS Catal.*, 2021, **11**, 12344–12354.

116 G. Kumar, R. S. Pillai, N. H. Khan and S. Neogi, *Appl. Catal., B*, 2021, **292**, 120149.

117 A. Jati, K. Dey, M. Nurhuda, M. A. Addicoat, R. Banerjee and B. Maji, *J. Am. Chem. Soc.*, 2022, **144**, 7822–7833.

118 J. Pang, Z. Di, J. Qin, S. Yuan, C. T. Lollar, J. Li, P. Zhang, M. Wu, D. Yuan, M. Hong and H. Zhou, *J. Am. Chem. Soc.*, 2020, **142**, 15020–15026.

119 H. Zhou, J. R. Long and O. M. Yaghi, *Chem. Rev.*, 2012, **112**, 673–674.

120 J. R. Long and O. M. Yaghi, *Chem. Soc. Rev.*, 2009, **38**, 1213–1214.

121 X. Cui, Z. Niu, C. Shan, L. Yang, J. Hu, Q. Wang, P. C. Lan, Y. Li, L. Wojtas, S. Ma and H. Xing, *Nat. Commun.*, 2020, **11**, 5456–5463.

122 V. Van Speybroeck and G. Maurin, *Nat. Mater.*, 2022, **22**, 12–13.

123 J. Wieme and V. Van Speybroeck, *J. Mater. Chem. A*, 2021, **9**, 4898–4906.

124 L. E. Kreno, K. Leong, O. K. Farha, M. Allendorf, R. P. Van Duyne and J. T. Hupp, *Chem. Rev.*, 2012, **112**, 1105–1125.

125 P. Horcajada, R. Gref, T. Baati, P. K. Allan, G. Maurin, P. Couvreur, G. Ferey, R. E. Morris and C. Serre, *Chem. Rev.*, 2012, **112**, 1232–1268.

126 Y. Li, Z. Fu and G. Xu, *Coord. Chem. Rev.*, 2019, **388**, 79–106.

127 W. P. Lustig, S. Mukherjee, N. D. Rudd, A. V. Desai, J. Li and S. K. Ghosh, *Chem. Soc. Rev.*, 2017, **46**, 3242–3285.

128 B. Li, M. Chrzanowski, Y. Zhang and S. Ma, *Coord. Chem. Rev.*, 2016, **307**, 106–129.

129 H. R. Moon, D. Lim and M. P. Suh, *Chem. Soc. Rev.*, 2013, **42**, 1807–1824.

130 D. Li, M. Kassymova, X. Cai, S. Zang and H. Jiang, *Coord. Chem. Rev.*, 2020, **412**, 213262–213277.

131 E. M. Johnson, S. Ilic and A. J. Morris, *ACS Cent. Sci.*, 2021, **7**, 445–453.

132 Q. Yang, Q. Xu and H. Jiang, *Chem. Soc. Rev.*, 2017, **46**, 4774–4808.

133 S. Cohen, *Nature*, 2019, **566**, 464–465.

134 W. Lu, Z. Wei, Z. Gu, T. Liu, J. Park, J. Park, J. Tian, M. Zhang, Q. Zhang, T. I. Gentle, M. Bosch and H. Zhou, *Chem. Soc. Rev.*, 2014, **43**, 5561–5593.

135 G. Lan, Y. Quan, M. Wang, G. T. Nash, E. You, Y. Song, S. S. Veroneau, X. Jiang and W. Lin, *J. Am. Chem. Soc.*, 2019, **141**, 15767–15772.

136 Y. Quan, G. Lan, Y. Fan, W. Shi, E. You and W. Lin, *J. Am. Chem. Soc.*, 2020, **142**, 1746–1751.

137 Z. Yan, M. Du, J. Liu, S. Jin, C. Wang, G. Zhuang, X. Kong, L. Long and L. Zheng, *Nat. Commun.*, 2018, **9**, 3353–3361.

138 L. Zeng, Z. Wang, Y. Wang, J. Wang, Y. Guo, H. Hu, X. He, C. Wang and W. Lin, *J. Am. Chem. Soc.*, 2019, **142**, 75–79.

139 Z. Yan, B. Ma, S. Li, J. Liu, R. Chen, M. Du, S. Jin, G. Zhuang, L. Long, X. Kong and L. Zheng, *Sci. Bull.*, 2019, **64**, 976–985.

140 Y. Song, Z. Li, Y. Zhu, X. Feng, J. S. Chen, M. Kaufmann, C. Wang and W. Lin, *J. Am. Chem. Soc.*, 2019, **141**, 12219–12223.

141 Y. Quan, Y. Song, W. Shi, Z. Xu, J. S. Chen, X. Jiang, C. Wang and W. Lin, *J. Am. Chem. Soc.*, 2020, **142**, 8602–8607.

142 X. Zhang, X. Wei, S. Huang and G. Yang, *Chem. – Asian J.*, 2021, **16**, 2031–2034.

143 K. Fan, W. Nie, L. Wang, C. Liao, S. Bao and L. Zheng, *Chem. – Eur. J.*, 2017, **23**, 6615–6624.

144 C. A. Kent, D. Liu, L. Ma, J. M. Papanikolas, T. J. Meyer and W. Lin, *J. Am. Chem. Soc.*, 2011, **133**, 12940–12943.

145 C. Wang and W. Lin, *J. Am. Chem. Soc.*, 2011, **133**, 4232–4235.

146 T. Devic and C. Serre, *Chem. Soc. Rev.*, 2014, **43**, 6097–6115.

147 M. Rimoldi, A. J. Howarth, M. R. DeStefano, L. Lin, S. Goswami, P. Li, J. T. Hupp and O. K. Farha, *ACS Catal.*, 2017, **7**, 997–1014.

148 B. Wang, X. Lv, D. Feng, L. Xie, J. Zhang, M. Li, Y. Xie, J. Li and H. Zhou, *J. Am. Chem. Soc.*, 2016, **138**, 6204–6216.

149 M. Liu, Y. Mu, S. Yao, S. Guo, X. Guo, Z. Zhang and T. Lu, *Appl. Catal., B*, 2019, **245**, 496–501.

150 X. Kong, Z. Lin, Z. Zhang, T. Zhang and W. Lin, *Angew. Chem., Int. Ed.*, 2016, **55**, 6411–6416.

151 M. Elcheikh Mahmoud, H. Audi, A. Assoud, T. H. Ghaddar and M. Hmadeh, *J. Am. Chem. Soc.*, 2019, **141**, 7115–7121.

152 C. Tan, X. Cao, X. Wu, Q. He, J. Yang, X. Zhang, J. Chen, W. Zhao, S. Han, G. Nam, M. Sindoro and H. Zhang, *Chem. Rev.*, 2017, **117**, 6225–6331.

153 J. I. Urgel, D. Ecija, W. Auwaerter, D. Stassen, D. Bonifazi and J. V. Barth, *Angew. Chem., Int. Ed.*, 2015, **54**, 6163–6167.

154 M. Zhao, Y. Huang, Y. Peng, Z. Huang, Q. Ma and H. Zhang, *Chem. Soc. Rev.*, 2018, **47**, 6267–6295.

155 G. Lan, Z. Li, S. S. Veroneau, Y. Zhu, Z. Xu, C. Wang and W. Lin, *J. Am. Chem. Soc.*, 2018, **140**, 12369–12373.

156 G. Lan, K. Ni, R. Xu, K. Lu, Z. Lin, C. Chan and W. Lin, *Angew. Chem., Int. Ed.*, 2017, **56**, 12102–12106.

157 Y. Zhang, J. Phipps and S. Ma, *Nat. Catal.*, 2022, **5**, 973–974.

158 Y. Quan, G. Lan, W. Shi, Z. Xu, Y. Fan, E. You, X. Jiang, C. Wang and W. Lin, *Angew. Chem., Int. Ed.*, 2021, **60**, 3115–3120.

159 P. I. Djurovich, D. Murphy, M. E. Thompson, B. Hernandez, R. Gao, P. L. Hunt and M. Selke, *Dalton Trans.*, 2007, 3763–3770.

160 D. GarciaFresnadillo, Y. Georgiadou, G. Orellana, A. M. Braun and E. Oliveros, *Helv. Chim. Acta*, 1996, **79**, 1222–1238.

161 A. Kobayashi, K. Shimizu, A. Watanabe, Y. Nagao, N. Yoshimura, M. Yoshida and M. Kato, *Inorg. Chem.*, 2019, **58**, 2413–2421.

162 A. Watanabe, A. Kobayashi, E. Saitoh, Y. Nagao, S. Omagari, T. Nakanishi, Y. Hasegawa, W. M. C. Sameera, M. Yoshida and M. Kato, *Inorg. Chem.*, 2017, **56**, 3005–3013.

163 A. Watanabe, A. Kobayashi, E. Saitoh, Y. Nagao, M. Yoshida and M. Kato, *Inorg. Chem.*, 2015, **54**, 11058–11060.

164 L. Li, S. Zhang, L. Xu, Z. Chen and J. Luo, *J. Mater. Chem. C*, 2014, **2**, 1698–1703.

165 T. Zhuo, Y. Song, G. Zhuang, L. Chang, S. Yao, W. Zhang, Y. Wang, P. Wang, W. Lin, T. Lu and Z. Zhang, *J. Am. Chem. Soc.*, 2021, **143**, 6114–6122.

166 X. Deng, J. Albero, L. Xu, H. Garcia and Z. Li, *Inorg. Chem.*, 2018, **57**, 8276–8286.

167 K. Wang, J. Zhang, Y. Hsu, H. Li, Z. Han, J. Pang, Z. Yang, R. Liang, W. Shi and H. Zhou, *Chem. Rev.*, 2023, **123**, 5347–5420.

168 L. Pan, M. Xu, L. Feng, Q. Chen, Y. He and B. Han, *Polym. Chem.*, 2016, **7**, 2299–2307.

169 O. M. Yaghi, *ACS Cent. Sci.*, 2019, **5**, 1295–1300.

170 M. Zhang, Y. Li, W. Yuan, X. Guo, C. Bai, Y. Zou, H. Long, Y. Qi, S. Li, G. Tao, C. Xia and L. Ma, *Angew. Chem., Int. Ed.*, 2021, **60**, 12396–12405.

171 Z. Mi, P. Yang, R. Wang, J. Unruangsri, W. Yang, C. Wang and J. Guo, *J. Am. Chem. Soc.*, 2019, **141**, 14433–14442.

172 H. Wang, Y. Yang, X. Yuan, W. Liang Teo, Y. Wu, L. Tang and Y. Zhao, *Mater. Today*, 2022, **53**, 106–133.

173 L. Akyuz, *Microporous Mesoporous Mater.*, 2020, **294**, 109850.

174 L. Bai, S. Z. F. Phua, W. Q. Lim, A. Jana, Z. Luo, H. P. Tham, L. Zhao, Q. Gao and Y. Zhao, *Chem. Commun.*, 2016, **52**, 4128–4131.

175 J. Á. Martín Illán, D. Rodríguez San Miguel, O. Castillo, G. Beobide, J. Perez Carvajal, I. Imaz, D. Maspoch and F. Zamora, *Angew. Chem., Int. Ed.*, 2021, **60**, 13969–13977.

176 X. Guan, F. Chen, Q. Fang and S. Qiu, *Chem. Soc. Rev.*, 2020, **49**, 1357–1384.

177 H. Fan, A. Mundstock, A. Feldhoff, A. Knebel, J. Gu, H. Meng and J. Caro, *J. Am. Chem. Soc.*, 2018, **140**, 10094–10098.

178 S. Xiong, L. Li, L. Dong, J. Tang, G. Yu and C. Pan, *J. CO_2* Util., 2020, **41**, 101224.

179 M. S. Lohse and T. Bein, *Adv. Funct. Mater.*, 2018, **28**, 1705553.

180 W. Liu, X. Li, C. Wang, H. Pan, W. Liu, K. Wang, Q. Zeng, R. Wang and J. Jiang, *J. Am. Chem. Soc.*, 2019, **141**, 17431–17440.

181 M. Wang, M. Ballabio, M. Wang, H. Lin, B. P. Biswal, X. Han, S. Paasch, E. Brunner, P. Liu, M. Chen, M. Bonn, T. Heine, S. Zhou, E. Canovas, R. Dong and X. Feng, *J. Am. Chem. Soc.*, 2019, **141**, 16810–16816.

182 Z. Meng, R. M. Stolz and K. A. Mirica, *J. Am. Chem. Soc.*, 2019, **141**, 11929–11937.

183 Y. Meng, Y. Luo, J. Shi, H. Ding, X. Lang, W. Chen, A. Zheng, J. Sun and C. Wang, *Angew. Chem., Int. Ed.*, 2020, **59**, 3624–3629.

184 L. Sun, M. Lu, Z. Yang, Z. Yu, X. Su, Y. Lan and L. Chen, *Angew. Chem., Int. Ed.*, 2022, **61**, e202204326.

185 J. L. Segura, S. Royuela and M. Mar Ramos, *Chem. Soc. Rev.*, 2019, **48**, 3903–3945.

186 S. Yang, W. Hu, X. Zhang, P. He, B. Pattengale, C. Liu, M. Cendejas, I. Hermans, X. Zhang, J. Zhang and J. Huang, *J. Am. Chem. Soc.*, 2018, **140**, 14614–14618.

187 J. Chen, X. Tao, C. Li, Y. Ma, L. Tao, D. Zheng, J. Zhu, H. Li, R. Li and Q. Yang, *Appl. Catal., B*, 2020, **262**, 118271–118278.

188 X. Zhao, P. Pachfule, S. Li, T. Langenhahn, M. Ye, C. Schlesiger, S. Praetz, J. Schmidt and A. Thomas, *J. Am. Chem. Soc.*, 2019, **141**, 6623–6630.

189 R. Bu, L. Zhang, L. Gao, W. Sun, S. Yang and E. Gao, *Mol. Catal.*, 2021, **499**, 111319–111327.

190 Z. Mi, T. Zhou, W. Weng, J. Unruangsri, K. Hu, W. Yang, C. Wang, K. A. I. Zhang and J. Guo, *Angew. Chem., Int. Ed.*, 2021, **60**, 9642–9649.

191 G. Kumar, M. Singh, R. Goswami and S. Neogi, *ACS Appl. Mater. Interfaces*, 2020, **12**, 48642–48653.

192 R. Liang and X. Zhao, *Org. Chem. Front.*, 2018, **5**, 3341–3356.

193 K. Huang, J. Zhang, F. Liu and S. Dai, *ACS Catal.*, 2018, **8**, 9079–9102.

194 Y. Zhao, Y. He and T. M. Swager, *ACS Macro Lett.*, 2018, **7**, 300–304.

195 B. J. Smith, A. C. Overholts, N. Hwang and W. R. Dichtel, *Chem. Commun.*, 2016, **52**, 3690–3693.

196 M. M. Unterlass, *Angew. Chem., Int. Ed.*, 2018, **57**, 2292–2294.

197 X. Li, C. Zhang, S. Cai, X. Lei, V. Altoe, F. Hong, J. J. Urban, J. Ciston, E. M. Chan and Y. Liu, *Nat. Commun.*, 2018, **9**, 2998–3005.

198 P. Wang, S. Ding, Z. Zhang, Z. Wang and W. Wang, *J. Am. Chem. Soc.*, 2019, **141**, 18004–18008.

199 Y. Luo, Z. Xu, H. Wang, X. Sun, Z. Li and D. Zhang, *ACS Macro Lett.*, 2020, **9**, 90–95.

200 Z. Xie, C. Wang, K. E. DeKrafft and W. Lin, *J. Am. Chem. Soc.*, 2011, **133**, 2056–2059.

201 H. Liang, Q. Chen and B. Han, *ACS Catal.*, 2018, **8**, 5313–5322.

202 W. Guo, H. Ding and B. Su, *J. Electroanal. Chem.*, 2018, **818**, 176–180.

203 T. R. Cook, Y. Zheng and P. J. Stang, *Chem. Rev.*, 2013, **113**, 734–777.

204 S. Zarra, D. M. Wood, D. A. Roberts and J. R. Nitschke, *Chem. Soc. Rev.*, 2015, **44**, 419–432.

205 H. Amouri, C. Desmarets and J. Moussa, *Chem. Rev.*, 2012, **112**, 2015–2041.

206 T. R. Cook and P. J. Stang, *Chem. Rev.*, 2015, **115**, 7001–7045.

207 Y. Liu, C. Hu, A. Comotti and M. D. Ward, *Science*, 2011, **333**, 436–440.

208 M. Fujita, M. Tominaga, A. Hori and B. Therrien, *Acc. Chem. Res.*, 2005, **38**, 369–378.

209 S. R. Seidel and P. J. Stang, *Acc. Chem. Res.*, 2002, **35**, 972–983.

210 O. Chepelin, J. Ujma, P. E. Barran and P. J. Lusby, *Angew. Chem., Int. Ed.*, 2012, **51**, 4194–4197.

211 O. Chepelin, J. Ujma, X. Wu, A. M. Z. Slawin, M. B. Pitak, S. J. Coles, J. Michel, A. C. Jones, P. E. Barran and P. J. Lusby, *J. Am. Chem. Soc.*, 2012, **134**, 19334–19337.

212 S. Oldknow, D. R. Martir, V. E. Pritchard, M. A. Blitz, C. W. G. Fishwick, E. Zysman-Colman and M. J. Hardie, *Chem. Sci.*, 2018, **9**, 8150–8159.

213 D. Rota Martir, D. Escudero, D. Jacquemin, D. B. Cordes, A. M. Z. Slawin, H. A. Fruchtl, S. L. Warriner and E. Zysman-Colman, *Chem. – Eur. J.*, 2017, **23**, 14358–14366.

214 S. Lamansky, P. Djurovich, D. Murphy, F. Abdel-Razzaq, H. Lee, C. Adachi, P. E. Burrows, S. R. Forrest and M. E. Thompson, *J. Am. Chem. Soc.*, 2001, **123**, 4304–4312.

215 H. Yersin, A. F. Rausch, R. Czerwieniec, T. Hofbeck and T. Fischer, *Coord. Chem. Rev.*, 2011, **255**, 2622–2652.

216 A. Ruggi, M. Berenguel Alonso, D. N. Reinhoudt and A. H. Velders, *Chem. Commun.*, 2010, **46**, 6726.

217 H. Sato, M. A. Blemker, G. Hellinghausen, D. W. Armstrong, J. W. Nafie, S. T. Roberts and M. J. Krische, *Chem. – Eur. J.*, 2019, **25**, 8719–8724.

218 S. Campagna, F. Puntoriero, F. Nastasi, G. Bergamini and V. Balzani, *Top. Curr. Chem.*, 2007, **280**, 117–214.

219 D. M. Schultz and T. P. Yoon, *Science*, 2014, **343**, 1239176–1239184.

220 B. Sahoo, J. Li and F. Glorius, *Angew. Chem., Int. Ed.*, 2015, **54**, 11577–11580.

221 A. G. Amador, E. M. Sherbrook and T. P. Yoon, *J. Am. Chem. Soc.*, 2016, **138**, 4722–4725.

222 L. Zhang and X. Hu, *Chem. Sci.*, 2017, **8**, 7009–7013.

223 A. Schultz, X. Li, B. Barkakaty, C. N. Moorefield, C. Wesdemiotis and G. R. Newkome, *J. Am. Chem. Soc.*, 2012, **134**, 7672–7675.

224 B. Laramee-Milette, F. Nastasi, F. Puntoriero, S. Campagna and G. S. Hanan, *Chem. – Eur. J.*, 2017, **23**, 16497–16504.

225 Z. Zhang, H. Wang, X. Wang, Y. Li, B. Song, O. Bolarinwa, R. A. Reese, T. Zhang, X. Wang, J. Cai, B. Xu, M. Wang, C. Liu, H. Yang and X. Li, *J. Am. Chem. Soc.*, 2017, **139**, 8174–8185.

226 J. Y. Ryu, E. H. Wi, M. Pait, S. Lee, P. J. Stang and J. Lee, *Inorg. Chem.*, 2017, **56**, 5471–5477.

227 C. Shen, A. D. W. Kennedy, W. A. Donald, A. M. Torres, W. S. Price and J. E. Beves, *Inorg. Chim. Acta*, 2017, **458**, 122–128.

228 K. Li, L. Zhang, C. Yan, S. Wei, M. Pan, L. Zhang and C. Su, *J. Am. Chem. Soc.*, 2014, **136**, 4456–4459.

229 S. Chen, K. Li, F. Zhao, L. Zhang, M. Pan, Y. Fan, J. Guo, J. Shi and C. Su, *Nat. Commun.*, 2016, **7**, 13169–13176.

230 K. Wu, K. Li, S. Chen, Y. Hou, Y. Lu, J. Wang, M. Wei, M. Pan and C. Su, *Angew. Chem., Int. Ed.*, 2020, **59**, 2639–2643.

231 J. Guo, Y. Xu, K. Li, L. Xiao, S. Chen, K. Wu, X. Chen, Y. Fan, J. Liu and C. Su, *Angew. Chem., Int. Ed.*, 2017, **56**, 3852–3856.

232 J. Guo, Y. Fan, Y. Lu, S. Zheng and C. Su, *Angew. Chem., Int. Ed.*, 2020, **59**, 8661–8669.

233 K. Li, K. Wu, Y. Lu, J. Guo, P. Hu and C. Su, *Angew. Chem., Int. Ed.*, 2022, **61**, e202114070.

234 D. Rota Martir, D. B. Cordes, A. M. Z. Slawin, D. Escudero, D. Jacquemin, S. L. Warriner and E. Zysman-Colman, *Chem. Commun.*, 2018, **54**, 6016–6019.

235 J. Tian, T. Zhou, S. Zhang, S. Aloni, M. V. Altoe, S. Xie, H. Wang, D. Zhang, X. Zhao, Y. Liu and Z. Li, *Nat. Commun.*, 2014, **5**, 5574–5584.

236 Y. Yamazaki, H. Takeda and O. Ishitani, *J. Photochem. Photobiol., C*, 2015, **25**, 106–137.

237 T. Koike and M. Akita, *Inorg. Chem. Front.*, 2014, **1**, 562–576.

238 S. Pullen, H. Fei, A. Orthaber, S. M. Cohen and S. Ott, *J. Am. Chem. Soc.*, 2013, **135**, 16997–17003.

239 K. Sasan, Q. Lin, C. Mao and P. Feng, *Chem. Commun.*, 2014, **50**, 10390–10394.

240 G. Lan, Y. Zhu, S. S. Veroneau, Z. Xu, D. Micheroni and W. Lin, *J. Am. Chem. Soc.*, 2018, **140**, 5326–5329.

241 S. Yang, B. Pattengale, S. Lee and J. Huang, *ACS Energy Lett.*, 2018, **3**, 532–539.

242 E. S. Sanz-Perez, C. R. Murdock, S. A. Didas and C. W. Jones, *Chem. Rev.*, 2016, **116**, 11840–11876.

243 Q. Schiermeier, *Nature*, 2011, **470**, 316.

244 J. Fu, K. Jiang, X. Qiu, J. Yu and M. Liu, *Mater. Today*, 2020, **32**, 222–243.

245 Z. Guo, G. Chen, C. Cometto, B. Ma, H. Zhao, T. Groizard, L. Chen, H. Fan, W. Man, S. Yiu, K. Lau, T. Lau and M. Robert, *Nat. Catal.*, 2019, **2**, 801–808.

246 D. Mellmann, P. Sponholz, H. Junge and M. Beller, *Chem. Soc. Rev.*, 2016, **45**, 3954–3988.

247 Y. Tamaki, T. Morimoto, K. Koike and O. Ishitani, *Proc. Natl. Acad. Sci. U. S. A.*, 2012, **109**, 15673–15678.

248 W. Zhu, C. Zhang, Q. Li, L. Xiong, R. Chen, X. Wan, Z. Wang, W. Chen, Z. Deng and Y. Peng, *Appl. Catal., B*, 2018, **238**, 339–345.

249 Y. Wang, N. Huang, J. Shen, P. Liao, X. Chen and J. Zhang, *J. Am. Chem. Soc.*, 2018, **140**, 38–41.

250 S. Chu, S. Fan, Y. Wang, D. Rossouw, Y. Wang, G. A. Botton and Z. Mi, *Angew. Chem., Int. Ed.*, 2016, **55**, 14260–14264.

251 Y. Nosaka and A. Y. Nosaka, *Chem. Rev.*, 2017, **117**, 11302–11336.

252 J. P. Celli, B. Q. Spring, I. Rizvi, C. L. Evans, K. S. Samkoe, S. Verma, B. W. Pogue and T. Hasan, *Chem. Rev.*, 2010, **110**, 2795–2838.

253 L. Li and B. Yeo, *Inorg. Chem.*, 2019, **58**, 7775–7784.

254 Y. Yu, S. Huang and G. Yang, *CrystEngComm*, 2022, **24**, 3160–3164.

255 A. P. Tuan, Y. Ping and G. Galli, *Nat. Mater.*, 2017, **16**, 401–408.

256 Y. Wan, L. Wang, H. Xu, X. Wu and J. Yang, *J. Am. Chem. Soc.*, 2020, **142**, 4508–4516.

257 Y. An, Y. Liu, P. An, J. Dong, B. Xu, Y. Dai, X. Qin, X. Zhang, M. Whangbo and B. Huang, *Angew. Chem., Int. Ed.*, 2017, **56**, 3036–3040.

258 L. Wang, Y. Wan, Y. Ding, S. Wu, Y. Zhang, X. Zhang, G. Zhang, Y. Xiong, X. Wu, J. Yang and H. Xu, *Adv. Mater.*, 2017, **29**, 1702428–1702435.

259 H. Hu, Z. Wang, L. Cao, L. Zeng, C. Zhang, W. Lin and C. Wang, *Nat. Chem.*, 2021, **13**, 358–366.

260 X. Wei, Y. Qi, S. Huang and G. Yang, *Eur. J. Inorg. Chem.*, 2022, e202200204.

261 X. Huang and E. Meggers, *Acc. Chem. Res.*, 2019, **52**, 833–847.

262 J. M. R. Narayanam and C. R. J. Stephenson, *Chem. Soc. Rev.*, 2011, **40**, 102–113.

263 J. Xuan and W. Xiao, *Angew. Chem., Int. Ed.*, 2012, **51**, 6828–6838.

264 S. Angerani and N. Winssinger, *Chem. – Eur. J.*, 2019, **25**, 6661–6672.

265 Y. Zhu, G. Lan, Y. Fan, S. S. Veroneau, Y. Song, D. Micheroni and W. Lin, *Angew. Chem., Int. Ed.*, 2018, **57**, 14090–14094.

266 J. Du, K. L. Skubi, D. M. Schultz and T. P. Yoon, *Science*, 2014, **344**, 392–396.

267 Z. Zuo, H. Gong, W. Li, J. Choi, G. C. Fu and D. W. C. MacMillan, *J. Am. Chem. Soc.*, 2016, **138**, 1832–1835.

268 H. Huo, X. Shen, C. Wang, L. Zhang, P. Roese, L. Chen, K. Harms, M. Marsch, G. Hilt and E. Meggers, *Nature*, 2014, **515**, 100–103.

269 H. Chen, W. Liu, A. Laemont, C. Krishnaraj, X. Feng, F. Rohman, M. Meledina, Q. Zhang, R. Van Deun, K. Leus and P. Van Der Voort, *Angew. Chem., Int. Ed.*, 2021, **60**, 10820–10827.

270 Z. Lu, G. B. Hammond and B. Xu, *Acc. Chem. Res.*, 2019, **52**, 1275–1288.

271 H. Zheng, Y. Fan, Y. Song, J. S. Chen, E. You, S. Labalme and W. Lin, *J. Am. Chem. Soc.*, 2022, **144**, 10694–10699.

272 D. Ma, Y. Zhang, S. Jiao, J. Li, K. Liu and Z. Shi, *Chem. Commun.*, 2019, **55**, 14347–14350.

273 S. P. Sancheti, Urvashi, M. P. Shah and N. T. Patil, *ACS Catal.*, 2020, **10**, 3462–3489.